PROTECT2024

9th International Colloquium on Performance, Protection & Strengthening of Structures Under Extreme Loading & Events

13 - 16 August 2024 I Singapore

CONFERENCE PROCEEDINGS

Organised by

NANYANG TECHNOLOGICAL UNIVERSITY SINGAPORE

NTU CEE Alumni Association

LIST OF TECHNICAL PAPERS

ID Number	Authors (s) – Paper Title
PS-59	***Weian Jiang, Haiyan Zhang, Lijun Yuan –*** Development Of Similarity Relationships For RC Columns Exposed To Non-uniform Fire Conditions
PS-64	***Lei Gao, Dan Gan, Xuhong Zhou, Pengfei He –*** Component-based mechanical models for square concrete-filled steel tubular diagonal-plate connections
PS-66	***Hadiseh Mohammadi, Dina Ghazi-nader, Min Sun, Sardar Malek*** – Reliability Of Finite Element Models For Numerical Analysis Of Strong Wood-frame Buildings Under Monotonic Loads
PS-67	***Ch. Hymavathi Annapoorna, G. Appa Rao –*** Calibration Of Concrete Damage Plasticity (CDP) Parameters For Numerical Analysis Of Reinforced Concrete Structure
PS-68	***Dina Ghazi-nader, Jacci Rock, Kyle Stueck, Roger Parra, Parham Khoshkbari, Sardar Malek -*** Finite Element Modeling Of Beam-to-column Connections In Tall Mass Timber Buildings

DEVELOPMENT OF SIMILARITY RELATIONSHIPS FOR RC COLUMNS EXPOSED TO NON-UNIFORM FIRE CONDITIONS

Weian Jiang[1], Haiyan Zhang[2], Lijun Yuan[3]

[1] Ph.D. candidate, School of Civil Engineering and Transportation, South China University of Technology, Guangzhou, P.R. China, weian.jiang@mail.scut.edu.cn

[2] Professor, State Key Laboratory of Subtropical Building and Urban Science, South China University of Technology, Guangzhou, P.R. China, zhanghy@scut.edu.cn

[3] Engineer, The Third Construction Engineering Co., Ltd. of China Construction Third Engineering Bureau, Guangzhou, P.R. China, 554142573@qq.com

Corresponding Author: Haiyan Zhang

South China University of Technology, Wushan Rd, Tianhe District, Guangzhou, P.R. China, 510641

Email: zhanghy@scut.edu.cn

ABSTRACT

The model fire test of reinforced concrete components often necessitates a furnace temperature-rising curve markedly exceeding that of the prototype, as prescribed by conventional similarity theory. Nonetheless, this prerequisite may occasionally render the model fire test unfeasible due to exceeding the heating capacity of the furnace. In response to this challenge, the present study conducts finite element analysis (FEA) on geometrically similar, reinforced, square concrete columns of various sizes exposed to fire from two or three sides, using the ISO 834 standard fire curve for all columns. The fire resistance results from FEA are utilized to derive similarity relationships for the time scale of the model to prototype columns. The similarity in the thermal-mechanical response of the model and prototype columns under the proposed time scale is evaluated and validated using experimental data from this study and previous research. The findings indicate that good similarity between the mechanical response and fire resistance of the model and prototype columns can be attained by normalizing the time scale using $s^{1.19}$ for 2-sided heating and $s^{1.29}$ for 3-sided heating, where s represents the geometric scale factor of model to prototype, the data from the model column under standard fire effectively predicts the axial deformation development and fire resistance of the prototype column.

Keywords: *Fire testing; Model testing; Reinforced concrete columns; Similarity; Fire resistance*

INTRODUCTION

The extensive utilization of concrete in high-rise constructions, coupled with the prevalence of fires, has elicited escalating global apprehension regarding the fire resilience of concrete structures. Laboratory furnace fire testing stands as a dependable method for ascertaining the fire endurance of components and structures. Nonetheless, spatial constraints inherent in conventional laboratory furnaces typically preclude the feasibility of conducting fire tests on large-scale components or full-scale structures. FEA conventionally serves as a means to forecast the fire performance of components or structures. However, the accuracy of FEA models necessitates validation through empirical test data. An alternative approach involves fire testing at a model scale, subsequently extrapolating to predict the fire resilience of a full-scale structure. That is usually the only practical way to predict the fire behavior of full-scale structures. Such methodologies inherently require the establishment of a robust similarity relationship to scale up the observed thermal and mechanical responses of the model to those of the prototype.

The mechanical response of a reinforced concrete (RC) member subjected to fire is intricately linked to its temperature distribution. Within the framework of traditional similarity theory, the attainment of highly similar temperature distributions between the prototype and model stands as a fundamental prerequisite for achieving similarity in their mechanical behaviors. Notably, in 1954, McGuire[1] elucidated the scaling law governing heat conduction, demonstrating that the duration required to establish comparable temperature distributions in geometrically similar members scales quadratically with the dimensional scale (s), provided that the time axis of the model's temperature-time curve is also scaled by s^2. Subsequently, McGuire extended the applicability of this scaling law to fire resistance. [2]. With a power exponent of 1.6–2.2 ($s^{1.6}$–$s^{2.2}$) the full-scale fire resistance of a beam could be predicted from that of a model beam.

Ng reported [3] the findings of fire experiments conducted on two scaled models (1:2.23 and 1:3) of RC columns, comparing the fire responses of the model columns subjected to a time-scaled fire curve with those of full-scale columns exposed to the ASTM standard fire curve. Due to the fact that the times of the fire curves for the models were scaled by s^2, a heating rate far higher than that of the prototype is required for the model. For example, the furnace temperature attained by the prototype within 60 minutes necessitated attainment within a mere 15 minutes for the 1:2 scale model. The intense fire for the 1:3-scale model column exceeded the furnace's operational capacity, resulting in discernible disparities between the experimental furnace temperature and the theoretical curve. Consequently, adjustments were requisite to rectify the fire endurance of the prototype forecasted from the 1:3-scale model test data utilizing the specified time scaling (s^2). Thus, it is evident that Ng's methodology exhibits limitations in scenarios characterized by significant disparities in scale between the model and the prototype.

Adjusting the temperature-rise curve for model fire testing can effectively ensure the thermal similarity between the model and prototype RC members. However, this adjustment often amplifies the challenges associated with fire testing, occasionally necessitating a heating rate that surpasses the capacity of the furnace. Conversely, if the fire resistance of the prototype and model can be maintained through the utilization of the same temperature-rise curve, model fire

testing becomes more feasible, although potentially resulting in non-identical temperatures between the prototype and the model. Reddy[4] conducted numerical simulations of geometrically-similar square columns exposed to a standard fire on all four sides and proposed a relative fire duration to relative size relationship of $s^{1.46}$ for square columns. However, Reddy's concept was not experimentally validated.

In the present study, a finite element model was developed and subsequently validated. Following this, parametric numerical simulations were conducted on both full-scale and reduced-scale columns, exposing them to non-uniform heating scenarios (3- and 2-sided fire exposure) and subjecting them to the ISO 834 standard fire curve. Subsequently, fire tests were performed to corroborate the numerical findings. The principal aim of the investigation was to establish a correlation between the fire resistance of columns of different scales. The outcomes of this study offer a practical model fire testing method, which can accurately predict the fire resistance of RC columns at full scale and mitigate the need for costly large-scale fire testing.

ESTABLISHMENT AND VALIDATION OF FINITE ELEMENT MODEL

The subsequent FEA was grounded on the empirical data provided by Wang[5]. Wang conducted fire experiments on an adjacent 2-sided heating column and a 3-sided heating column, both featuring a section size of 300 × 300 mm and a height of 3810 mm. In the ensuing analysis, FEA was carried out on these two columns, with adjustments made and subsequent validation undertaken through a comparative assessment between the FEA outcomes and the experimental results. Following validation, parametric investigations were conducted on columns of various scales. Based on the findings derived from these parametric studies, similarity relationships governing the fire resistance of columns with differing scales were delineated.

Establishment of FEA model

FEA was conducted utilizing the commercial software ABAQUS. Truss elements were employed to simulate the behavior of the steel bars, while C3D8R elements were selected to model the concrete material. The interface between the steel bars and concrete was designated as an "embedded region," thereby disregarding any potential slip between the two materials. Boundary conditions were applied to both ends of the column: the upper end was configured with pinned connections enabling axial translation and rotation, whereas only rotation was permitted at the lower end. Pertinent thermal properties, including specific heat and conductivity, were sourced from Lie's published works [6,7] for both concrete and steel. Thermal expansion coefficients were derived from Eurocode 2 [8]. The concrete's mechanical response was governed by a concrete damage plasticity model [9] , while an elastic-plasticity model was employed for the steel bars. Stress-strain relationships were defined according to Guo's formulation [10] for concrete and Eurocode 2 [8] for steel. The thermal-mechanical analysis was executed through sequential coupling, with the mechanical analysis contingent upon the thermal analysis outcomes.

Validation of FEA model

Figure 1 and Figure 2 shows the comparison between tested results in Wang's[5] research and in FEA. It can be seen that the temperature variation and the fire resistances between the tested and simulated results are close. Consequently, the thermal and mechanical parameters would be adopted for subsequent parametric studies.

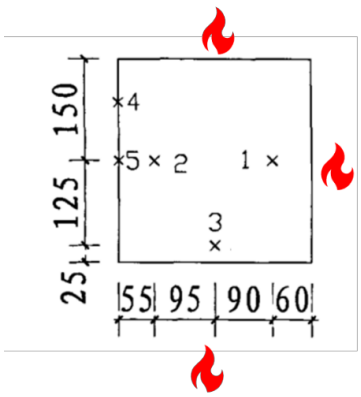

(a) Thermocouple locations of 3-sided heating column in Wang[5]

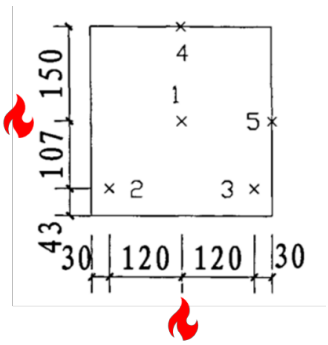

(b) Thermocouple locations of 2-sided heating column in Wang[5]

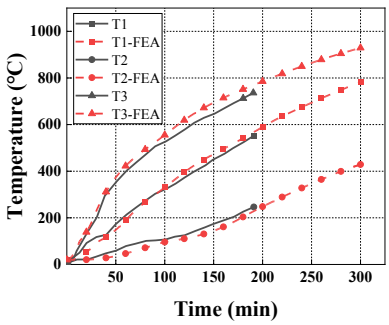

(c) Temperature variation of 3-sided heating

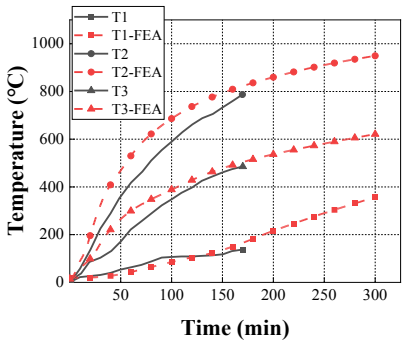

(d) Temperature variation of 2-sided heating

Figure 1 Thermocouple locations and temperature variation in Wang's[5] experiment and in FEA results

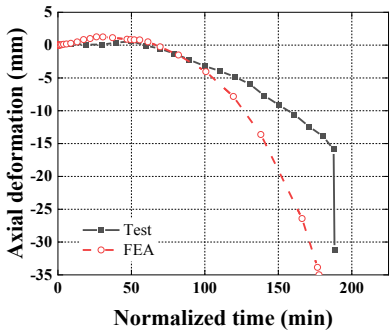

(a) 3-sided heating

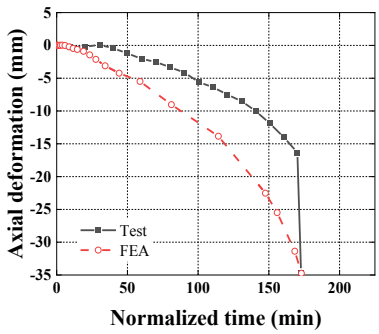

(b) 2-sided heating

Figure 2 Axial deformation evolution in Wang's[5] experiment and in FEA results

Parametric study

Based on the validated thermal and mechanical properties, parametric studies were performed in columns with varying scales. 0.5-, 0.6-, 0.7-, 0.8-, 0.9- and 1.0- scale columns, were modeled. Their dimensions were proportional to the prototype columns (as depicted in Figure 3), while the reinforcement ratio, load ratio, furnace temperature curve and boundary condition remained unchanged. Scale greater than 1.0 was not considered since the 1.0-scale column was taken as the prototype column. Table 1 summarizes the fire resistances assuming 2-sided and 3-sided fire exposure. The table shows that with a given heating mode the fire resistance of a column increases with its size, but not linearly.

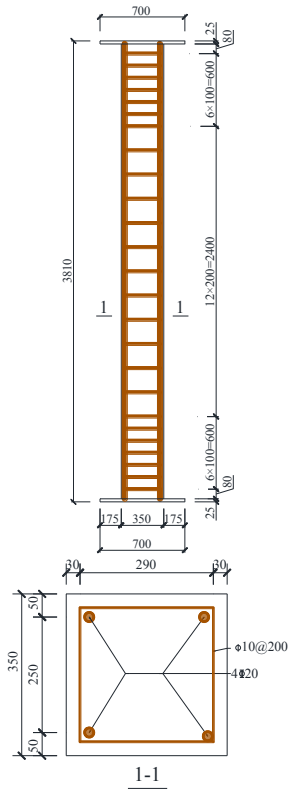

Figure 3 Geometric sizes and reinforcement of the prototype columns

Table 1 Fire resistance in FEA results

Heating mode	Scale	Fire resistance
		FEA (min)
2-sided	0.5	186
	0.6	214
	0.7	271
	0.8	286
	0.9	333
	1.0	363
3-sided	0.5	114

0.6	130
0.7	172
0.8	184
0.9	220
1.0	285

DEVELOPING OF SIMILARITY RELATIONSHIP

Based on the fire resistance of the FEA, a similarity relationship quantifying the relative fire resistance of prototype and model columns can be obtained by regression analysis. This similarity relationship, as the time scale, should also apply to the development of the temperature distribution and axial deformation.

Developing the similarity relationship

Reddy [4] have proposed the following model to describe the relationship between the fire resistances of two similar square RC columns exposed to fire on all four sides and their size scale.

$$\frac{t_{\mathrm{p}}}{t_{\mathrm{m}}} = \left(\frac{l_{\mathrm{p}}}{l_{\mathrm{m}}}\right)^{x} = s^{x} \qquad (1)$$

where t_{m} and t_{p} are the fire resistances in model and full scale; l_{m} and l_{p} are their characteristic sizes and x is called the time-similarity index. Reddy proposed that x is 1.46 with square columns and 4-sided heating [4]. Using the form of Eq. (1) and the data in Table 1 , the time-similarity indexes for 2-sided and 3-sided heating can be estimated by regressing the fire resistances against the scale. Figure 4 presents the results for both 2-sided and 3-sided heating. The regressions suggest indexes for 2- and 3-sided heating of 1.19 and 1.29. The R^2 values are 0.990 and 0.987, respectively, so the regressed curves fit the data points well, as shown in Figure 4. A published curve and data points for 4-sided heating [4] are also plotted. It shows that as the number of heated sides decreases, the value of the time-similarity index decreases, and the relationship between the relative fire resistance and the relative size tends to be linear. This implies that the size-induced difference in fire resistance of square RC columns decreases with the number of sides heated.

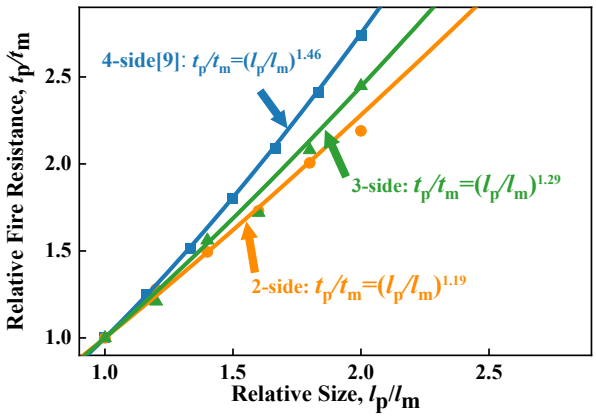

Figure 4 Relative fire resistance (t_p/t_m) vs. relative size (l_p/l_m)

Similarity analysis of sectional average temperature evolution

The similarity relationship of fire resistance is commonly regarded as the time scale [2]. Using this similarity relationship to scale the time axis, the thermal and mechanical response of the model columns can be normalized, which enables the comparison on the similarity between the thermal-mechanical response of the model and prototype. For example, adjusting the horizontal (time) axis of the measured temperature-time curves of the model columns with 3-sided fire exposure by dividing $s^{1.29}$ while keeping the vertical (temperature) axis unchanged (the similarity factor of temperature being 1), and this is called the normalized procedure.

FEA gives temperatures at each of the mesh nodes, from which sectional average temperatures can be calculated. Figure 5 compares the sectional average temperatures of columns at 0.5-, 0.7- and 1.0 scale at the columns' mid-height section. The time axis is normalized using $s^{1.19}$ and $s^{1.29}$ for 2- and 3-sided heating columns, respectively. The sectional average temperature evolution of the three columns with different scales and under the same heating mode is very close.

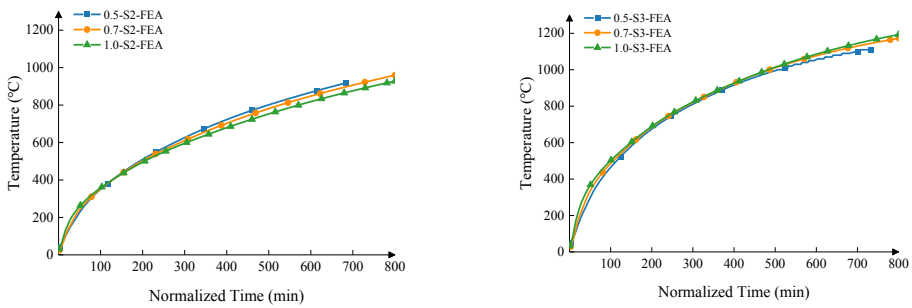

(a) 2-sided heating (b) 3-sided heating

Figure 5 Sectional average temperature evolution with 2- and 3-sided heating under normalized time

Figure 6 illustrates the normalized axial deformation evolution of 2- and 3-sided heating columns under normalized time scale. It can be seen that both the deformation patterns and fire resistance exhibit notable similarity across columns of varying scales following normalization.

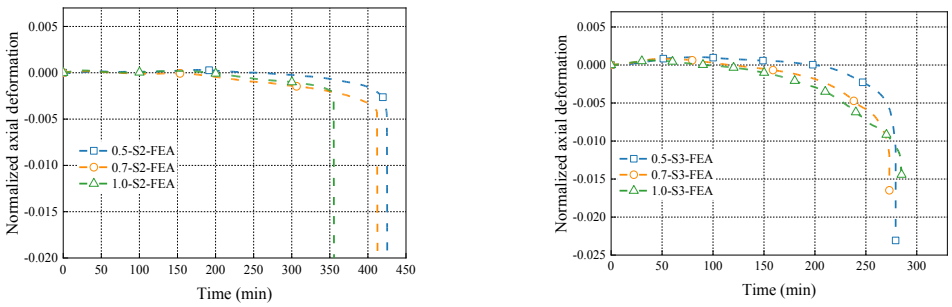

(a) 2-sided heating (b) 3-sided heating

Figure 6 Normalized axial deformation evolution with 2- and 3-sided heating under normalized time

EXPERIMENTAL VALIDATION

Test overview

The present study's fire tests focused on six square RC columns, constructed at scales of 0.5, 0.7 and full scale. They were exposed to fire on two or three sides. The specimens were denoted as 0.5-S2, 0.5-S3, 0.7-S2, 0.7-S3, 1.0-S2 and 1.0-S3, where the number before the hyphen is the geometric scale and number after the hyphen refers to the number of sides exposed to fire. Prototype columns (1.0-S2, 1.0-S3) measured 350mm × 350mm in cross-section and were 3810mm in height, with 2600mm exposed to the fire. The geometric dimensions of the model columns are scaled to 0.7 and 0.5 times that of the prototype columns. Additionally, the longitudinal reinforcement ratio in the model-scale columns remained nearly constant, ranging between 0.54% and 0.56%. Similarly, the volumetric stirrup ratios were maintained at nearly equivalent levels, ranging from 1.08% to 1.12% in the middle. Moreover, the thickness of the concrete cover was scaled proportionately. All of the columns were fabricated from the same batch of commercial siliceous aggregate concrete. The average compressive strength of six 150mm concrete cubes was 36.1MPa at the time of the fire tests.

All of the columns were subjected to an axial load equal to 35% of their bearing capacity at ambient temperature. The bearing capacities were calculated using the actual material strength tested on the day of the fire test. The load was kept constant throughout the test. All of the columns were exposed to the ISO 834 standard fire. The columns were instrumented with thermocouples and displacement transducers. Axial deformation was measured at the top of the columns using four symmetrically distributed linear variable differential transducers (LVDTs). During the tests, the applied load, upper end displacement and temperature were recorded in real-time. According to Chinese national code GB/T 9978.1-2008 [11], the failure criterion was defined as either $h/100$ (axial deformation, where h is the heated length) or $3h/1000$mm/min (deformation rate).

Test results

Figure 7 depicts the average axial deformation progression of the six columns during the fire, as measured by the four LVDTs installed at the tops of the columns. As illustrated in the figure, the axial deformation initially exhibits a positive (tensile) trend attributable to thermal expansion, gradually transitioning to negative (compressive deformation) as the elevated temperature compromises the strength of the concrete and steel. Subsequently, as a column becomes incapable of sustaining the load, its axial deformation experiences a rapid increase, signifying the reaching of its fire resistance limit. The fire resistance values for all columns are detailed in Table 2 . It should be noted that column 1.0-S2 did not fail even after 5 hours of exposure.

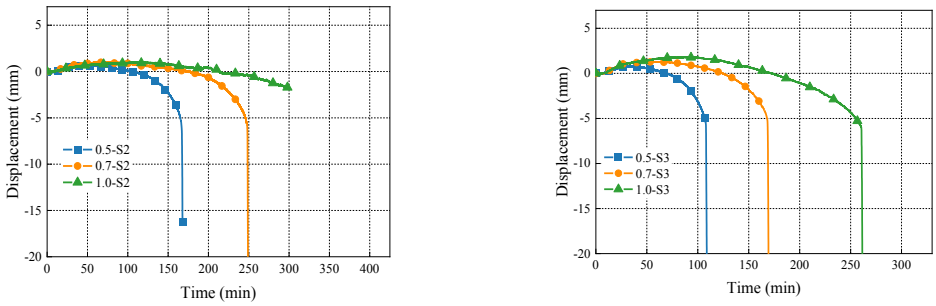

(a) 2-sided heating columns (b) 3-sided heating columns

Figure 7 Axial deformations evolution during fire tests

Table 2 Summary of the specimen parameters and test results

Specimen No.	0.5-S2	0.5-S3	0.7-S2	0.7-S3	1.0-S2	1.0-S3
Fire resistance (min)	166	107	248	167	>300	262

Similarity of mechanical response

Normalized axial deformation curves can be derived using a similar procedure—normalizing the time axis using $s^{1.19}$ or $s^{1.29}$ for 2-sided and 3-sided heating respectively. The measured deformations can be normalized by dividing by the heated length of the column. Figure 8 (a) and (b) show the normalized axial deformation – time curves for columns heated on 2 and 3 sides with three scales. In each case the three normalized curves are quite close, further validating the similarity relationship proposed by FEA.

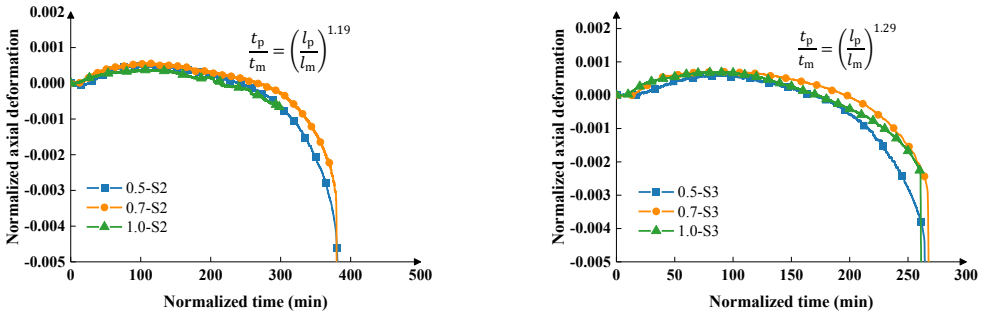

(a) 2-sided heating (b) 3-sided heating

Figure 8 Normalized axial deformation variation with normalized time

CONCLUSIONS

FEA and fire tests on 2- and 3-sided heating columns with different geometric scales, were conducted in this paper. The time scales of columns under the two heating modes were proposed and validated, and the similarity in thermal-mechanical response of prototype and model columns was evaluated. Based on the results from FEA and experiments, the following conclusions can be drawn:

(1) Achieving a completely similar sectional temperature distribution to that of the prototype is not a prerequisite for conducting model fire tests. As long as the model and prototype columns have similar average sectional temperatures, good similarity between the mechanical response of the model and prototype can be achieved. Therefore, the same fire curve can be used for the model and prototype fire tests.

(2) Under the ISO 834 standard fire, the ratio of the fire resistance of a model square RC column to that of a similar full-scale column varies as about $s^{1.19}$ for 2-sided heating and $s^{1.29}$ for 3-sided fire exposure, where s is geometric scale factor.

ACKNOWLEDGMENTS

This research was supported by China's National Natural Science Foundation (grant No. 51978286) and the Natural Science Foundation of Guangdong Province (grant No. 2020A1515010728). That support is gratefully acknowledged. Any opinions, findings, conclusions or recommendations expressed in this paper are those of the authors and do not necessarily reflect the views of the sponsors.

REFERENCES

[1] J. H. McGuire (1954) The scaling of dimensions in heat conduction problems. *Fire Research Notes*. 94.

[2] J. H. McGuire, W. W. Stanzak, and Margaret Law (1975) The scaling of fire resistance problems. *Fire Technology*. 11 (3), 191–205.

[3] M. Saeed Mirza, and T. T. Lie Ah Book N. G (1990) Response of Direct Models of Reinforced Concrete Columns Subjected to Fire. *ACI Structural Journal*. 87 (3),.

[4] Dronnadula V. Reddy, Khaled Sobhan, Lixian Liu, and Jody D. Young (2015) Size effect on fire resistance of structural concrete. *Engineering Structures*. 99 468–478.

[5] Chao, W. (2006) Study on fire resistance of RC columns with different faces exposed to fire, Master, South China University of Technology, 2006.

[6] T. T. Lie and T. D. Lin (1985) Fire performance of reinforced concrete columns. *Fire Safety: Science and Engineering*.

[7] T. T. Lie (1994) Fire resistance of circular steel columns filled with bar-reinforced concrete. *Journal of Structural Engineering*. 120 (5), 1489–1509.

[8] EN1992-1-2, Eurocode2 (2004) Design of concrete structures - Part 1-2: General Rules - Structural Fire Design. European Committee for Standardization, Brussels.

[9] J. Lubliner, J. Oliver, S. Oller, and E. Oñate (1989) A plastic-damage model for concrete. *International Journal of Solids and Structures*. 25 (3), 299–326.

[10] Guo, Z. and Shi, X. (2011) Experiment and calculation of reinforced concrete at elevated temperatures. Butterworth-Heinemann, .

[11] GB/T9978.1—2008 (2008) Fire-resistance tests-elements of building construction Part1: General Requirements. Standardization Administration of China, Beijing.

Component-based mechanical models for square concrete-filled steel tubular diagonal-plate connections

Lei Gao[1], Dan Gan[2], Xuhong Zhou[3], Pengfei He[4]*

[1] School of Civil Engineering, Chongqing University, 1406862722@qq.com.

[2] School of Civil Engineering and Geomatics, Southwest Petroleum University, gand03@qq.com.

[3] School of Civil Engineering, Chongqing University, zhouxuhong@126.com.

[4] School of Civil Engineering, Chongqing University, 15537898976@163.com.

Corresponding Author: Dan Gan, PhD, Professor.

Southwest Petroleum University, Chengdu, China, 610500. **Email:** gand03@qq.com.

ABSTRACT

This work proposes a square concrete-filled steel tubular (CFST) joint system, in which vertically placed diagonal plates help transfer the tensile load from the beam flanges. The CFST diagonal-plate connections were experimentally investigated under tension. The failure mode was analyzed based on the test results. The CFST diagonal-plate connections achieved the beam end failure mode, and the stress concentration at the steel tube corners obviously relieves. The Void Growth Model (VGM) model was used to predict the fracture of each specimen, and it showed high accuracy compared with the experimental results, which verified the applicability of the VGM model for predicting the entire process of forces of the CFST diagonal-plate connections under tensile load. Component-based models have been developed and used for predicting the initial stiffness and strength of the CFST diagonal-plate connections. The hand calculation procedures for yield and ultimate deflection were also developed. The load–deformation curve consists of three segments: the first represents the elastic behavior from the classic plate theory, the second is obtained by plotting the deformation at the ultimate strength against the maximum load, and the third is a horizontal line stretching to the failure point. The mechanical models were compared with test and numerical simulation results, and good agreement was shown between them.

Keywords: *Tensile Behaviour, Diagonal Plate, Void Growth Model, Component Model, Initial Stiffness, Strength.*

1. INTRUCTION

CFST columns possess high load capacity, large stiffness, and good ductility owing to the composite action between the steel tube and the in-filled concrete [1], and they are widely used in mid- and high-rise buildings, in which the behavior of composite beam-to-column connections is crucially important in terms of both the load transfer and structural details.

Arranging transverse diaphragm plates is one of the most effective ways to transfer both the tension and compression forces from beam flanges to the CFST joint region. The interior-diaphragm, through-diaphragm, and exterior-diaphragm connections are most commonly used in practice [2] (Figure. 1).

Interior-diaphragm connection (Figure 1a) is commonly used for large-sized CFST columns, mainly due to the welding between an interior diaphragm and the steel tube is inconvenient and the quality of concrete pouring was not easy to ensure. Exterior-diaphragm connections are easy to construct (Figure 1b), and the quality of concrete pouring in the joint region can be easily ensured. However, the exterior diaphragm will occupy the building space, and the amount of steel used for the exterior diaphragm is large [3]. Through-diaphragm connection (Figure 1c) combines the characteristics of the two types of connections, but the steel tube must be disconnected at the connection, which brings additional workload to the installation of building components [4].

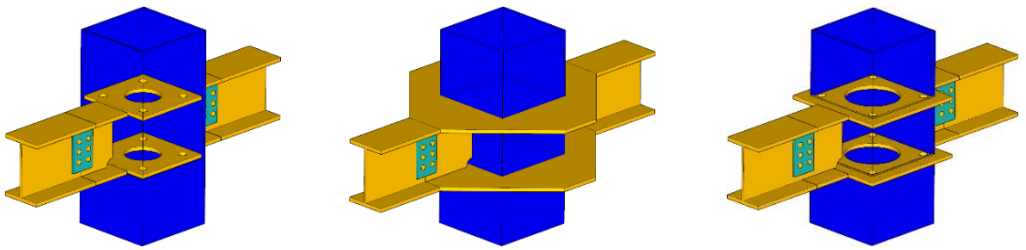

(a) Interior-diaphragm connection (b) Exterior-diaphragm connection (c) Through-diaphragm connection

Figure 1. Three types of CFST beam-to-column connections (Infilled concrete is not shown).

For the above reasons, the diagonal-plate connections are proposed in this work, in which diagonal plates are vertically arranged in the joint region to avoid taking up the exterior space and ensure concreting quality (Figure. 2). Two construction schemes can be adopted: the first scheme is to cut openings in a structural steel tube, and then insert diagonal plates into the openings and weld them. Then weld corbels with extended steel beam flanges, pour concrete, and finally connect the steel beam. The other scheme is to weld diagonal plates inside a cold-formed U-shaped plate, and then weld two U-shaped plates together to form a steel tube. The remaining steps are the same as the first construction scheme.

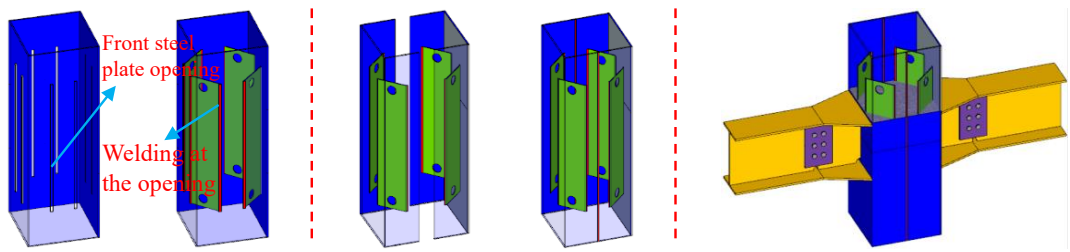

Cut opening Weld diagonal plate Weld diagonal plate Form steel tube diagonal-plate connection

First scheme of construction Second scheme of construction

Figure. 2. Two types of installation process for diagonal plates

Doung et al. [5] conducted tensile tests on square interior-diaphragm connections, investigated the effects of infill concrete and geometry of the interior-diaphragm on the mechanical properties of the joints. Miao et al. [6] conducted tensile tests on through-diaphragm CFST connections, investigated the influence of the geometry of the through diaphragm, and proposed formulas for calculating the load-carrying capacity. Zhu et al. [7] experimentally and numerically investigated the tensile behavior of exterior-diaphragm CFST connections stiffened with PBL, and explored their tensile load transfer paths.

To analyze the tensile performance of the diagonal-plate connections, this work conducted tensile tests on square CFST column-to-steel beam connections with diagonal-plate. The failure mode was analyzed. A finite element model (FEA) considering steel fracture was established. The initial stiffness and strength model of the connections was established based on component models. Calculated values were compared to the experimental and numerical simulation results for both initial stiffness and strengths to evaluate the accuracy of the model.

2 EXPERIMENTAL PROGRAMS

2.1 Specimen design

The failure of welded CFST joints mainly depends on the details of the connection between the tensile flange of the steel beam and the column tube, while during earthquakes the failure might feature the fracturing of the connection if it were not reasonably designed; thus, three CFST diagonal-plate connection specimens (CJD-100-8-100-6, CJD-100-8-200-6, and CJD-100-8-200-6*) were designed and tested to evaluate the tensile behavior (Figures. 3). The nomenclature of specimen begins with the letters CJD, followed by information of the width and thickness of beam flange. The following numbers represented the height and thickness of diagonal plate. Note that * represented the second construction scheme as shown in Figures. 2.

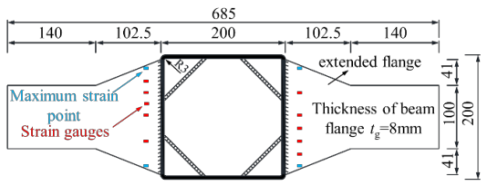

(a) Plan

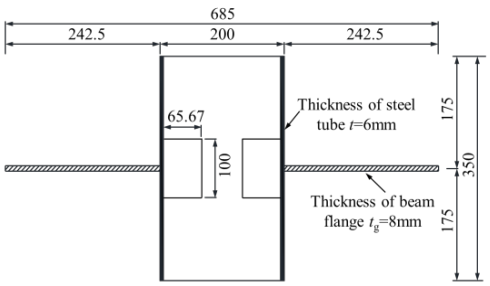

(b) Elevation

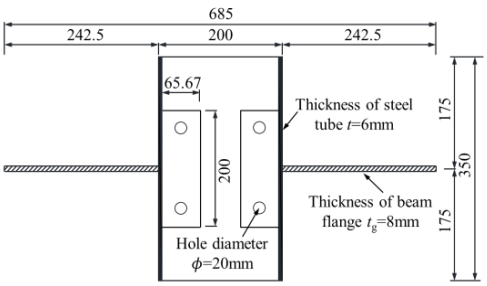

(c) Elevation

Figure 3. Details and dimensions of specimens with diagonal-plate (Unit in mm)

2.2 Material properties

Six 150 mm × 150 mm × 150 mm concrete cubes, made and cured with the same conditions with the specimens, were used to measure the concrete strength. The average cubic compressive strength was 50.2 MPa.

The steel tubes and diagonal plates with a thickness of 6 mm. The beam flange plate with a thickness of 8 mm. Three coupons were tested to obtain the Young's modulus (E_s), yielding strength (f_y), and ultimate strength (f_u), as shown in Table 1.

Table 1. Material properties of steel

Measured thickness t (mm)	Yielding strength f_y (MPa)	Ultimate strength f_y (MPa)	Young's modulus E_s (MPa)
5.5	298	443	186982
7.4	289	430	185768

To simulate the fracture of steel, the test was also conducted on smooth round bar specimens (R0) and circumferentially notched tensile (CNT) coupon specimens (R2, R5, and R8). All specimens were taken from the beam flange plate, and the dimensions of the specimens are shown in Figure 4. The specimens R2, R5, and R8 represent the circumferential notch radius of 2mm, 5mm, and 8mm, respectively. The design of three types of CNT coupon specimens was referred to literature [8]. The load-displacement curve of the specimens was shown in Figure 5.

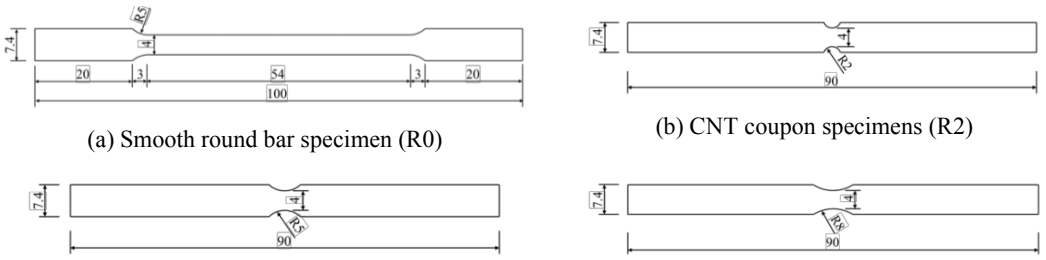

(a) Smooth round bar specimen (R0)

(b) CNT coupon specimens (R2)

(c) CNT coupon specimens (R5)

(d) CNT coupon specimens (R8)

Figure 4. Specimen layout (unit: mm)

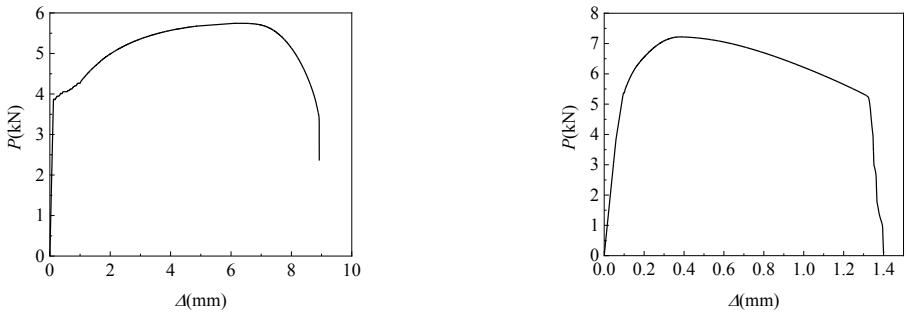

(a) The specimen of R0

(b) The specimen of R2

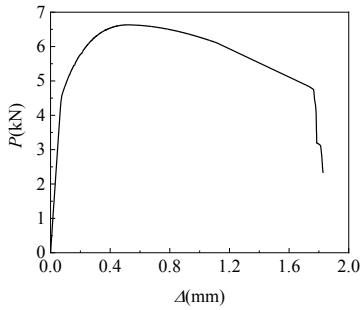

(c) The specimen of R5

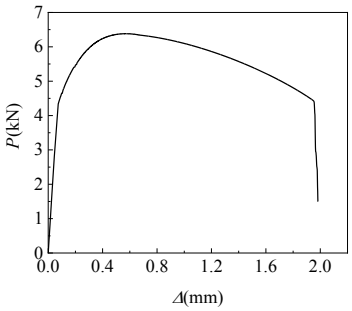

(d) The specimen of R8

Figure 5. Load-deformation curves of specimens

3 FAILURE MODES

The CFST diagonal-plate connections (CJD-100-8-100-6, CJD-100-8-200-6) failed by the yielding and followed fracturing of the beams as shown in Figure. 6(a) and (b). They showed almost no observable out-of-plane deformation in the joint region. When the beam flange yielded and then the deformation increased continuously, and the paint peeled off at the beam flange end. When the tensile load reached the peak load, the beam flange cracked and continued to develop with necking. There was neither damage of the joint region nor of the welds till the end of testing. The diagonal plates made the stress distribution more uniform in the extended flange, which relieved the stress concentration at the steel tube corners.

For the CFST diagonal-plate connection constructed by the second scheme (CJD-100-8-200-6*), the specimen failed because of the fracturing of the welds after the beam flange yielded as shown in Figure. 6(c)). The reason is that only one side of the diagonal plates was welded, and when the welds fractured, more tension would be transferred through the steel tube corners, which resulted in severe stress concentration and followed cracking of the welds at the steel tube corners.

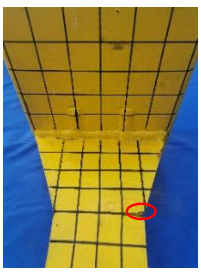

(a) CJD-100-8-100-6

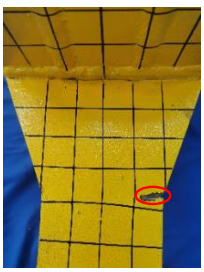

(b) CJD-100-8-200-6

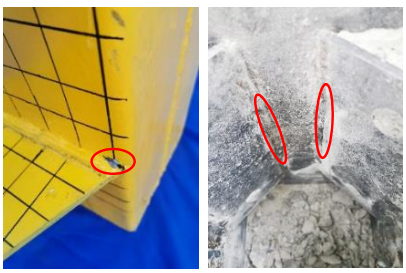

(c) CJD-100-8-200-6*

Figure 6. Failure modes of specimens

4 FINITE ELEMENT MODEL VALIDATION

4.1 Material model

A complete plastic model should comprise the yield criterion, the hardening law, and the flow law. The Von-Mises yield function was used as material yield criterion [9].

The true stress–strain relationship is required to simulate the force–displacement curve and fracture evolution, which can be transformed from the following equations.

$$\sigma_{\text{ture}} = \alpha(K(\varepsilon_0 + \varepsilon_{\text{eqp}})^{n_1} + (1-\alpha)(\sigma_{\text{y0}} + Q(1 - e^{-m\cdot\varepsilon_{\text{eqp}}^{n_2}})) \quad (1)$$

where α is a weight coefficient; ε_{eqp} is plastic true strain; ε_0 is the first yielding strain; K and n_1 are two unknown constant parameters; σ_{y0} is yield stress; B, m_1 and n_2 are unknown constants.

The parameter was calculated by a trial-and-error method until the simulation results agreed well with the experimental results. The material parameters of Swift and HS hardening models were shown in Table 2. Besides, the associated flow law was adopted.

Table 2. The material parameters of hardening law

Swift-HS mixed hardening criterion					
α	K	n_1	Q	m_1	n_2
0.42	855.40Mpa	0.23	219.90Mpa	59.51	1.38

4.2 Solid FE model

For the sake of better computing efficiency, only a 1/4 part of at tensile specimen (R0, R2, R5, and R8) was modelled, because there were two symmetrical planes. All the finite element models were built with the reduced integration 8-node brick element (C3D8R).

A mesh dependency assessment was performed. Different element sizes (0.1 mm, 0.2 mm, 0.3 mm, 0.4 mm, and 0.5 mm) were evaluated to find a balance between accuracy and efficiency. A fine element size of 0.2 mm was selected for the gauge area, and a 0.5 mm element was chosen for the rest parts of each specimen. This grid layout cannot only ensure calculation accuracy but also save calculation time.

4.3 Evaluation of ductile fracture models

The VGM [10] model simulate the fracture of steel. The VGM model is based on an exponential relationship between the void growth rate and stress triaxiality, which reads

$$\varepsilon_{\text{eqp}}^{\text{f}}(T) = \begin{cases} \infty & T \le 0 \\ \eta e^{-\beta T} & 0 \le T \end{cases} \quad (2)$$

where $\varepsilon_{\text{eqp}}^{\text{f}}$ is critical equivalent plastic strain at fracture initiation; T is triaxiality; β and η is material property constant.

A commonly-used linear damage accumulation law was adopted, as expressed by

$$D = \int \frac{1}{\varepsilon_{\mathrm{eqp}}^{\mathrm{f}}} d\varepsilon_{\mathrm{eqp}} \tag{3}$$

where D is accumulated damage. When D reaches unity, the element will be deleted.

4.4 Q235 steel fracture parameters

In the process of metal plastic deformation, stress triaxiality, and the lode parameter keep changing with the increase of equivalent plastic strain. Averaged stress triaxiality was given by Eq. (4), which considered the effect of loading history on damage accumulation. The average stress triaxiality and the equivalent plastic strain at fracture of each type specimen are listed in Table 3. The calibrated parameters (η and β) of the VGM model were 1.83 and 0.75, respectively.

Table 3. The average stress triaxiality and the equivalent plastic strain at fracture.

Specimen	Average stress triaxiality	Equivalent plastic strain
R0	0.590	1.157
R2	0.774	1.081
R5	0.827	0.947
R8	1.013	0.849

4.5 Fracture simulation of material specimens

Figure 7 shows the comparison of load-displacement curves between finite element simulation and test results of smooth round bar and CNT coupon specimens based on the VGM model. As shown in Figure 7, the fracture location obtained from finite element simulation was in good agreement with the test results, indicating that the VGM model could accurately predict the ductile fracture behavior of Q235 steel under tensile load.

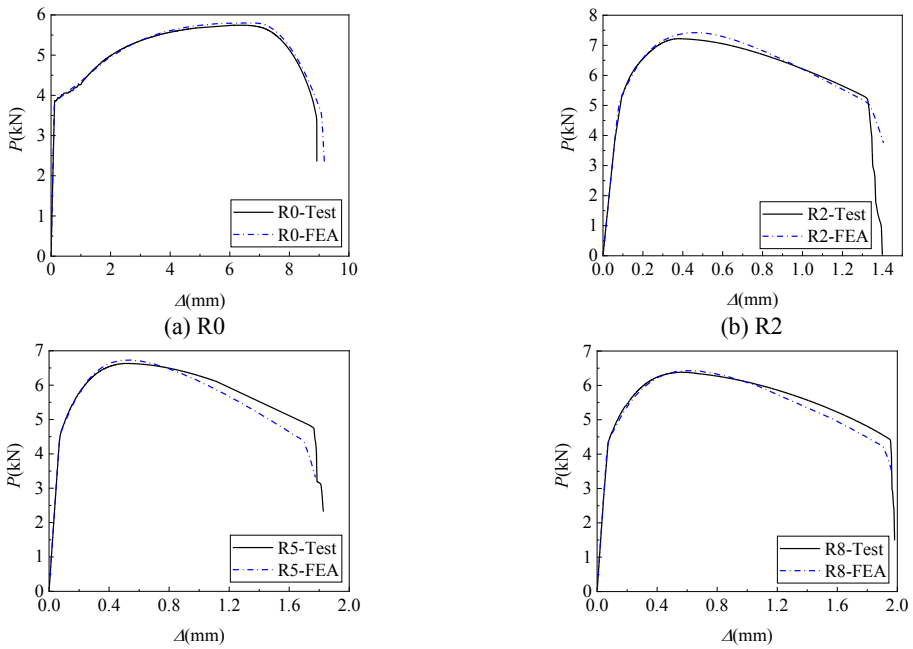

Figure 7. Comparison of load-deformation curves between experimental and numerical simulations

4.6 Fracture simulation of CFST diagonal-plate connection

In addition to the CFST diagonal-plate connections in this paper, the simulations were also conducted on the same batch of CFST diagonal-plate connections as in this paper. The load-displacement curves of all connection specimens were shown in Figure 8. The numerical simulation curve was good agree with the experimental curve.

The yield strength, ultimate strength, and fracture displacement of the connection specimens were shown in Table 4. The average values of yield strength, ultimate strength, and fracture displacement between simulation and test results are 1.03, 1.03, and 0.98, respectively.

Thus, the VGM model can accurately predict the trend of the curve of CFST diagonal-plate connections. The VGM model can be used to expand connection parameters and provide data support for subsequent component model validation.

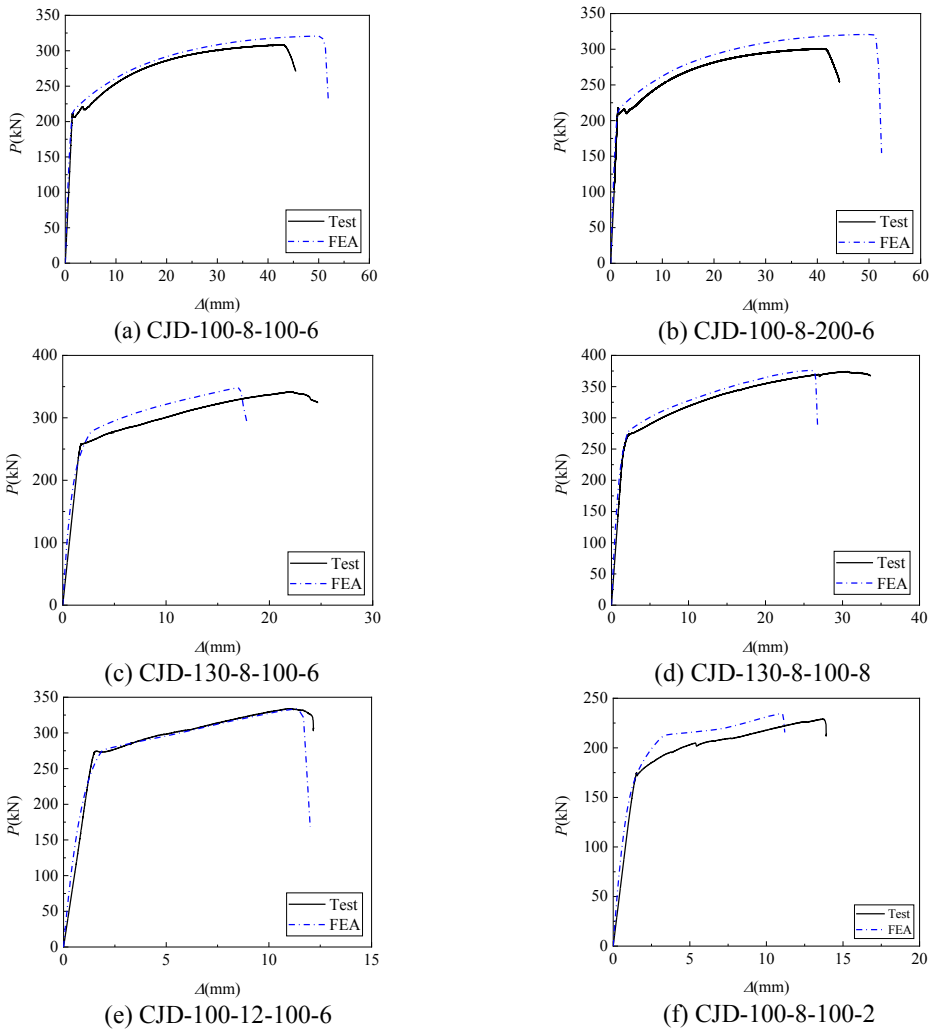

Figure 8. Comparisons between experimentally and numerically obtained load-deformation curves

Table 4. Summary of test and simulation results.

Specimens	Yield strength (kN)		Ultimate strength (kN)		Fracture displacement (mm)	
	Test	Simulation	Test	Simulation	Test	Simulation
CJD-100-8-100-6	207.5	213.9	308.3	320.7	42.9	50.2
CJD-100-8-200-6	209.8	213.9	300.5	320.7	40.9	50.7
CJD-130-8-100-6	256.3	278	341.6	349	22	17.2
CJD-130-8-100-8	273.7	278	373.7	375.9	30.7	26.2
CJD-100-12-100-6	274.2	275.5	334	334.2	10.9	11.3
CJD-100-8-100-2	180.4	180	228.5	234.4	13.7	11

5. COMPONENT-BASED MODELS FOR DIAGONAL-PLATE CONNECTIONS

5.1 Model of initial stiffness of diagonal-plate connections

When the ratio of the width of the extended flange to the width of the steel tube was greater than 0.85, the tensile load was considered directly transmitted to the steel tube webs. The deformation of the joint region was dominated by the tensile deformation of the steel tube webs within a certain length range. Therefore, the initial stiffness of the connection can be obtained by calculating the tensile stiffness of the steel tube webs, and the connection between the extended flange and the steel tube was simplified as a rigid body [11].

For CFST diagonal-plate connections, the steel tube flange provided stiffness through out-of-plane deformation, but the stiffness of in-plane deformation was much greater than that of out-of-plane deformation. Therefore, the contribution of out-of-plane deformation of the steel tube flange to stiffness is ignored, and the contribution of the steel tube webs and diagonal plates to stiffness is considered.

The deformation of the joint region was mainly caused by the steel tube webs and the diagonal plates within a certain length range, and the effective lengths of connections were l_{e1} and l_{e2}, respectively. The initial stiffness model of the CFST diagonal-plate connections could be regarded as the superposition of the stiffness of steel tube webs and the stiffness of diagonal plates, as shown in Figure 9.

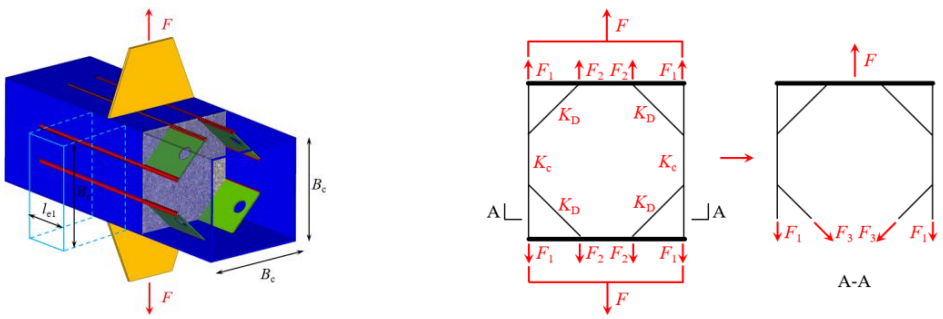

Figure 9. Mechanical model of initial stiffness of CFST diagonal-plate connections

The Hooke's law in material mechanics was used to calculate the simplified model, as expressed by Eq (4)

$$K_0 = \frac{F}{\Delta} = \frac{2E_1 l_{e1} t_b}{B_c} + \frac{3\sqrt{2}E_2 l_{e2} t_d}{B_c} \tag{4}$$

where E_1 and E_2 were elastic modulus of the steel tube webs and the diagonal plates, respectively; l_{e1} and l_{e2} were the effective lengths of the steel tube webs and the diagonal plates, respectively; t_b and t_d were the thickness of the steel tube webs and the diagonal plates, respectively; B_c was the width of the steel tube.

The effective length l_e of the connection was defined as the range of forces that the steel tube web and diagonal plate participate in longitudinally during the initial loading stage, that is, the effective length of the steel tube web and diagonal plate was related to force transmission ratio. Due to the use of maximum strain in the simplification process of Eq (4), it is necessary to convert the longitudinal stress distribution direction into a certain range of uniform stress to reach the maximum longitudinal stress through Eq (5).

$$l_e = \frac{\int_0^l \sigma \mathrm{dx}}{\sigma_{max}} \tag{5}$$

where l_e was the effective length of the steel tube web and the diagonal plate, respectively; σ_{max} was the maximum longitudinal stress.

To calculate the effective length of connections, a parametric analysis method is adopted as shown in Table 7. To save calculation time, static analysis is used in finite element software for calculation. The steel strength was unified at 235MPa and the elastic modulus was 206000MPa.

The dimensions of steel tube 200×200×6mm, beam flange 120×6mm, and diagonal plate 100×6mm were used as reference specimens. Through the finite element analysis, the influence factor of the effective length of the connection included the width of the beam flange B_b, the thickness of the beam flange t_b, the thickness of steel tube t_c, and the thickness of diagonal plate t_d. The calculation formula for the effective length of the steel tube webs can be obtained through regression analysis as follows:

$$l_{e1} = 0.05B_b + 0.78t_b - 0.44t_c - 0.49t_d \tag{6}$$

Using the same regression method, the formula for calculating the effective length of diagonal plates was as follows:

$$l_{e2} = 0.02B_b + 0.48t_b + 0.28t_c - 0.25t_d \tag{7}$$

The comparison between the theoretical formula results and the finite element results of The CFST diagonal-plate connections was shown in Figure 10, with a mean of 0.98 and a standard deviation of 0.04, indicating that the formula had high accuracy.

Garifulin et al. [12] pointed out that the initial axial stiffness of connections did not need to be as precise as the bearing capacity, and a deviation of 30% was allowed in engineering design. The comparison between the theoretical calculated values and test values of The CFST diagonal-plate connections was shown in Figure 10, with a mean of 0.92 and a standard deviation of 0.09, indicating a good agreement between the theoretical formula and test values.

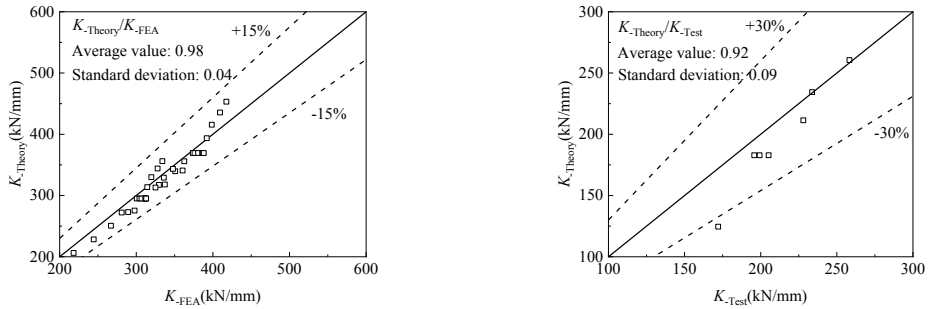

(a) Theoretical formulas and numerical simulations (b) Theoretical formulas and test

Figure 10. The comparison of initial stiffness

5.2 Model of yield strength of diagonal-plate connections

We used the component model method [13] to solve the contributions of the steel tube and the diagonal plate, respectively.

5.2.1 Contribution of the diagonal plate

The yield tension capacity of the diagonal plate can be calculated by multiplying the effective transmission length with the yield strength. The effective transmission length was defined as the stress of the diagonal plate reaching yield within a certain length range.

$$P_{y1} = f_{yd} l_d t_d \tag{8}$$

where f_{yd} was the yield strength of the diagonal plate; l_d was the effective transmission length, and t_d was the thickness of the diagonal plate.

Using the same regression analysis method as Formula 9, the formula for calculating the effective length of the steel tube web was as follows:

$$l_{ed} = (0.21B_b + 1.5t_b + 1.33t_c - 2.7t_d) \times \left(\frac{0.26f_{yb}}{235} - \frac{0.61f_{yc}}{235} - \frac{1.1f_{yd}}{235} + 3.38\right) \tag{9}$$

where f_{yb}, f_{yc} and f_{yd} were the yield strength of the beam flange, the steel tube, and the diagonal plate.

5.2.2 Contribution of the steel tube

The width of steel tube was equal to that of the beam flange, and the flexural capacity analysis model can be assumed based on the yield line mechanism, as shown in Figure. 11.

The strength of I-beam to column connections loaded by in-plane bending moments under $B_b = B_c$ condition was derived by [13] as

$$M_y = 2(t_b + 5t_c) f_{yc} t_c (h_b - t_b) \tag{10}$$

where t_b and t_c were the thickness of beam flange and steel tube, respectively; h_b was the distance of resisting forces of beam.

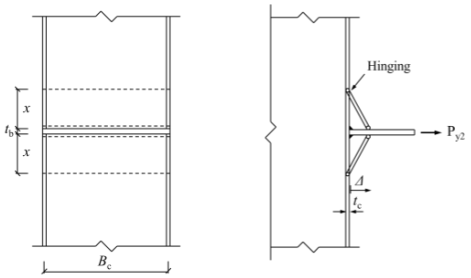

Figure 11. Flexural capacity analysis model under $B_b = B_c$ condition.

Therefore, the yield tension capacity of the steel tube can also be calculated by the traditional method as

$$P_{y2} = 2(t_b + 5t_c)f_{yc}t_c \tag{11}$$

5.3 Yielding and ultimate deformation

The yield deformation (w_y) can be calculated by dividing the yield load by the initial stiffness

$$w_y = \frac{P_y}{K_0} = \frac{P_{y1} + P_{y2}}{K_0} \tag{12}$$

In this paper, the ultimate deformation limit (w_u) proposed by Jones and Wang [14] for the concrete-filled RHS connections was adopted, which can be determined by Eq. (13).

$$w_u = \begin{cases} 6\%B_c & \text{when } t_c/B_c \le 0.05 \\ (13 - 140\dfrac{t_c}{B_c}) & \text{when } 0.05 < t_c/B_c < 0.075 \\ 2.5\%B_c & \text{when } t_c/B_c \ge 0.075 \end{cases} \tag{13}$$

5.4 Load–deformation relationship

The load–deformation curve of the connection can be approximated as trilinear having a yield strength point and an ultimate strength point as shown in Figure. 12.

The yield strength point in this model is based on the superposition of the contribution of the steel tube (P_{y1}), and diagonal plate (P_{y2}), given by Eq. (14)

$$P_y = P_{y1} + P_{y2} \tag{14}$$

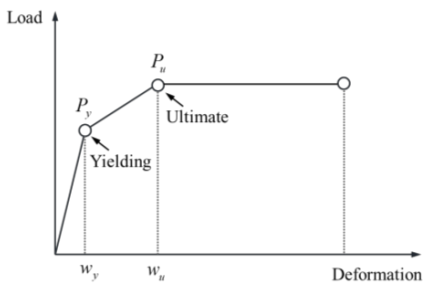

Figure. 12. Assumed trilinear load–deformation skeleton curves of diagonal-plate connections.

The corresponding yield deformation is given in Eq. (12).

The yield strength of steel (f_y) is multiplied by a factor (k_β) to reflect the effect of strain hardening. Therefore, the ultimate strength (P_u) may be calculated by Eq. (15) and the corresponding deformation is given in Eq. (13).

$$P_u = P_{u1} + P_{u2} = l_{ed} k_\beta f_{yd} + 2(t_b + 5t_c) k_\beta f_{yc} t_c \tag{15}$$

where k_β was is defined as the average ratio of ultimate bearing capacity to yield bearing capacity in the test of connection failure, which was 1.30.

For the connection specimens CJD-100-8-100-6 and CJD-100-8-200-6, the failure mode of the connections was beam end failure, and the theoretical yield bearing capacity of the beam flange was used instead of the theoretical yield bearing capacity of the connections.

To validate the accuracy of the proposed formulae above, the results calculated by the theoretical methods are compared with the test and numerical simulation ones as given in Figure 13. The failure mode of finite element simulation was connection failure.

The ratio of connection failure of the predicted yield and ultimate strength to experimental and finite element results was 1.02 and 0.99, respectively. Thus, the formulae proposed in the present study show good agreement with observed values from tests and finite elements.

It should be noted that the theoretical ultimate deformation of the CFST connection with diagonal-plate was smaller than that of the test and finite element. This is because the theoretical ultimate deformation value in this paper was proposed by Jones and Wang [14] based on the rectangular concrete-filled steel tubular connections with no stiffener, and the diagonal plate can significantly reduce stress concentration at the steel tube corners and enhance the ductility of the connection.

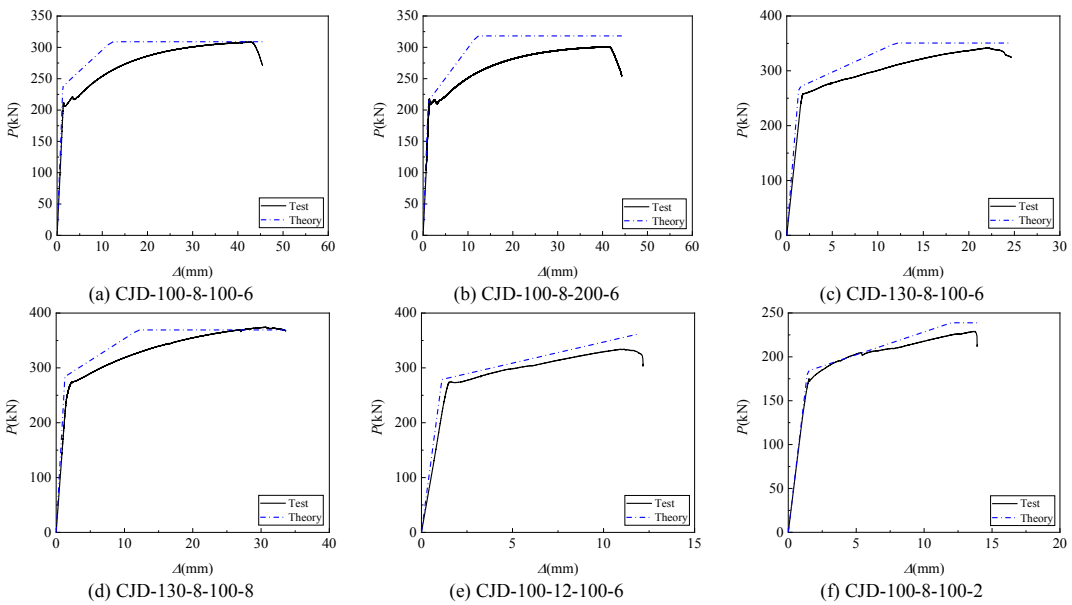

(a) CJD-100-8-100-6 (b) CJD-100-8-200-6 (c) CJD-130-8-100-6

(d) CJD-130-8-100-8 (e) CJD-100-12-100-6 (f) CJD-100-8-100-2

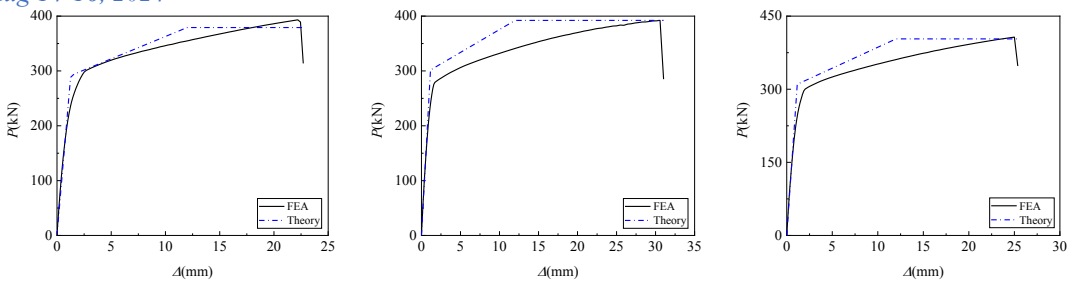

(g) CJD-140-8-100-8 (h) CJD-130-8-100-10 (i) CJD-140-8-100-10

Fig. 13. Comparison of predicted and test and finite element results.

6. CONCLUSION

1. The proposed the CFST diagonal-plate connections can achieve the beam failure, which is characterized by yielding and followed fracturing of the beam flange, and the joint region is not damaged; the equal strength design principle should be used for determining the weld size, i.e., the weld size will be the size where the weld strength is at least equal to the diagonal-plates strength.
2. The VGM model can accurately predict the trend of the curve of the CFST diagonal-plate connections. The VGM model can be used to expand connection parameters.
3. The use of the proposed theoretical model led to good agreement between the predicted and test and finite element load–deformation curves.

ACKNOWLEDGMENTS

The research in this paper was funded by the National Natural Science Foundation of China (No. 52378133) and the Chongqing Natural Science Foundation (No. 2023NSCQ-MSX3013). The authors wish to express their gratitude to the sponsors.

REFERENCES

[1] Li, S., & Han, LH. (2018). Concrete-encased CFST columns under combined compression and torsion: Analytical behavior. *Journal of Constructional Steel Research*, 144: 236–52.

[2] Xu, X., & Cheng, R. (2022). Experimental study of U-shaped steel-concrete composite beam to square CFST column joints. *Journal of Constructional Steel Research*, 192: 107220.

[3] CECS 28: 2012. Technical specification for concrete-filled steel tubular structures [S]. *Beijing: China Planning Press*, 2012. (in Chinese)

[4] JGJ 99−2015. (2016). Technical specification for steel structure of tall building [S]. *Beijing: China Architecture & Building Press*. (in Chinese)

[5] Doung, P., & Sasaki, E. (2019). Load-deformation characteristics and performance of internal diaphragm connections to box columns. *Thin-Walled Structures*, 143: 106221.

[6] Miao, JK., & Jiang, XL. (2009). Static tensile test on diaphragm-through joints of concrete-filled square steel tubular column. *Journal of Tianjin University*, 42(3):208–13. (in Chinese)

[7] Zhu, WQ., & Mo, ZP. (2021). Tensile behavior and load transfer mechanism of concrete-filled square steel tube exterior-diaphragm connections stiffened with PBL. *Engineering Structures*, 231: 111780.

[8] Lou, YS., & Chen, L. (2017). Modeling of ductile fracture from shear to balanced biaxial tension for sheet metals. *International Journal of Solids and Structures*, 112: 169-184.

[9] Xu, BY. (2005). *Applied Elastoplastic Mechanics*. Beijing, Tsinghua University Press. (in Chinese)

[10] Rice, JR., & Tracey, DM. (1969). On ductile enlargement of voids in triaxial stress fields. *Journal of the Mechanics and Physics of Solids*, 17(3): 201–17.

[11] Mo, ZP. (2021). Research on the tensile performance of PBL reinforced rectangular steel tube concrete joints. *Chang'an University*. (in Chinese)

[12] Garifullin, M., & Bronzova, M. (2019). Initial axial stiffness of welded RHS T joint. *Journal of Constructional Steel Research*, 153: 459-472.

[13] Lu, LH. (1997). *The static strength of I-beam to rectangular hollow section column connections*. Netherlands, Delft Univ. Press.

[14] Jones, MH., & Wang, YC. (2010). Tying behaviour of fin-plate connection to concrete-filled rectangular steel tubular column–Development of a simplified calculation method. *Journal of Constructional Steel Research*, 66(1): 1-10.

RELIABILITY OF FINITE ELEMENT MODELS FOR NUMERICAL ANALYSIS OF STRONG WOOD-FRAME BUILDINGS UNDER MONOTONIC LOADS

Hadiseh Mohammadi[1], Dina Ghazi-nader[2], Min Sun[3], Sardar Malek[4]

[1] Graduate student, Department of Civil Engineering, University of Victoria, Canada, E-mail address: hadisehmohammadi@uvic.ca

[2] Graduate student, Department of Civil Engineering, University of Victoria, Canada, E-mail address: dina@uvic.ca

[3] Associate Professor, Department of Civil Engineering, University of Victoria, Canada, E-mail address: msun@uvic.ca

[4] Assistant Professor, Department of Civil Engineering, University of Victoria, Canada, E-mail address: smalek@uvic.ca

Corresponding Author: Hadiseh Mohammadi, M.Sc.

Department of Civil Engineering, University of Victoria, 3800 Finnerty Rd, Victoria, BC V8P 5C2, Canada

Email: hadisehmohammadi@uvic.ca

ABSTRACT

Conventional wood-frame shear walls with and without hold-down devices are often used in low-rise wood frame buildings across North America. For mid-rise buildings, especially those located in high seismic zones, stronger shear walls with strong hold-down systems comprising continuous steel rods are employed to manage overturning moments. Although the performance of low-rise wood buildings under seismic loads is well understood, research on structural performance and failure mechanisms of mid-rise buildings with strong wood-frame shear walls is still limited. Due to the high cost of conducting experimental research on a mid-rise building, this paper is aimed to explore finite element (FE) models for better understanding of the behaviour of stronger wood-frame shear walls under gravity and lateral loads. To elucidate the performance of strong shear walls and validating the accuracy of the developed models, a one-story strong wood-frame shear wall with different hold-down systems is modelled in two commercial finite element software (i.e. ABAQUS and SAP2000) under lateral loading. To compare numerical models and determine the limitations of each model, capacity curve of the strong walls under monotonic load are predicted. Unlike most FE models in which modelling parameters are calibrated, real connection and material properties are used as input parameters. Results show a good agreement between the models' predictions and existing experimental results in terms of wall deflection and capacity curve. Some limitations in capturing the pinching effects are noted using the same input parameters for connections. Hence, further research on predicting the cyclic response of strong shear walls is suggested.

Keywords: *Strong wood-frame shear walls, Finite element method, Continuous steel rod, Discrete hold-down, Monotonic load*

INTRODUCTION

Wood-frame construction is among popular construction methods for building mid-rise apartments in North America. Shear wall is an essential structural component in carrying lateral loads in such building. Hence, it requires further attention for building taller, resilient wood-frame buildings. Wood shear walls consist of studs, sheathing, and fasteners typically nails, with visually graded lumber members serving as studs and plates. The sheathing panel is attached to the stud wall with nails (on one or both sides) and plays a key role in increasing the shear stiffness and strength and serves as lateral support for the studs. The combination of panels with studs and plates creates an efficient lateral force resistance system. To connect the shear wall to the floor below or to the foundation, and prevent overturning of the whole wall system, hold-down devices are typically used at the corners of the walls.

As the seismic demands are increasing in new version of codes and guidelines, a wall configuration with a higher capacity is often necessary to resist the larger vertical and horizontal forces. Higher-capacity shear walls are typically built using, stronger end studs, and stronger hold-down devices, sheathing panels on both sides of the wall, more nails with a reduced nailing space or more rows of nails [1]. These design elements result in a more robust and effective lateral force resistance system, capable of resisting the increased loads in mid-rise structures.

To estimate the stiffness and calculate the deflection of wood-frame shear walls, simple analytical models have been developed in the literature [2]. It is worth mentioning that such equations are derived based on mechanics-based approaches to describe the deformation behaviour of light-frame wood shear walls proposed first in 1952 [3]. The accuracy of such equations has been validated based extensive testing programs in the USA and Canada conducted on conventional low-capacity shear walls. However, the relevance of such equations for higher-capacity shear walls (e.g. exceeding nominal strength of 100 kN) has been less-investigated. Recently, Guíñez et al. [4] examined the monotonic and cyclic lateral response of 17 strong wood frame walls with different geometry and nail spacings. Results showed that strong walls with discrete hold-downs and smaller nail spacings have an increased capacity and delayed stiffness degradation. However, it was also found that the Special Design Provisions for Wind and Seismic (SDPWS) [5] design equation overestimates the stiffness of strong wood frame walls. Similarly, Estrella et al. [6] showed that the SDPWS design provisions underestimate the strengths and overestimate the stiffnesses of strong walls with continuous steel rod hold-downs.

Reviewing literature highlights that despite the established knowledge on the nonlinear behaviour of conventional shear walls, there is limited research examining the deformation response of strong wood-frame shear walls. The objectives of this study are to: (i) develop a reliable numerical tool to study the deformation response of strong shear walls; and (ii) assess the accuracy of the design equations presented in the Canadian Standards Association (CSA) [7] in calculating the deflection of such walls.

Methodology

Two strong shear wall configurations are selected and modelled in two FE software packages. The walls consist of studs, top plates, bottom plates, foundations, sheathing panels, framing-to-framing nail connections, and sheathing-to-framing nail connections as shown in Figure 1 and 2. All framing members were constructed using 38 × 135 mm dimensional lumber from Radiata pine. The walls were sheathed on both sides using 11.1 mm thick OSB panels, measuring 1220 mm in width and 2400 mm in height. The mechanical properties of the studs and sheathing material (OSB) are listed in Table 1. The wall configuration comprised seven studs spaced at 400 mm on center. End-studs consisted of four members each, while both the bottom and top plates were composed of double members. Further details of the selected shear walls can be found in [1].

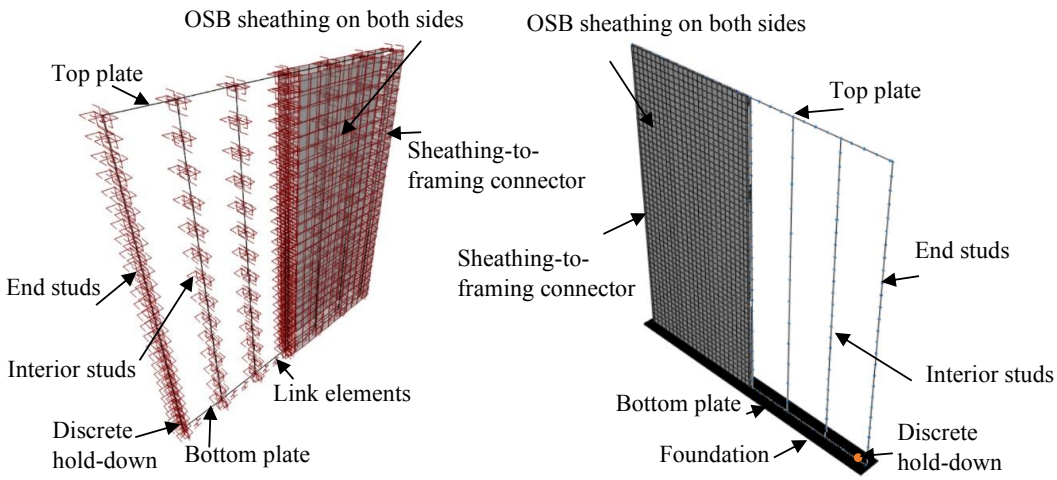

Figure 1. Schematic of finite element model of strong light-frame wood walls with discrete hold-downs: (a) SAP2000, (b) ABAQUS.

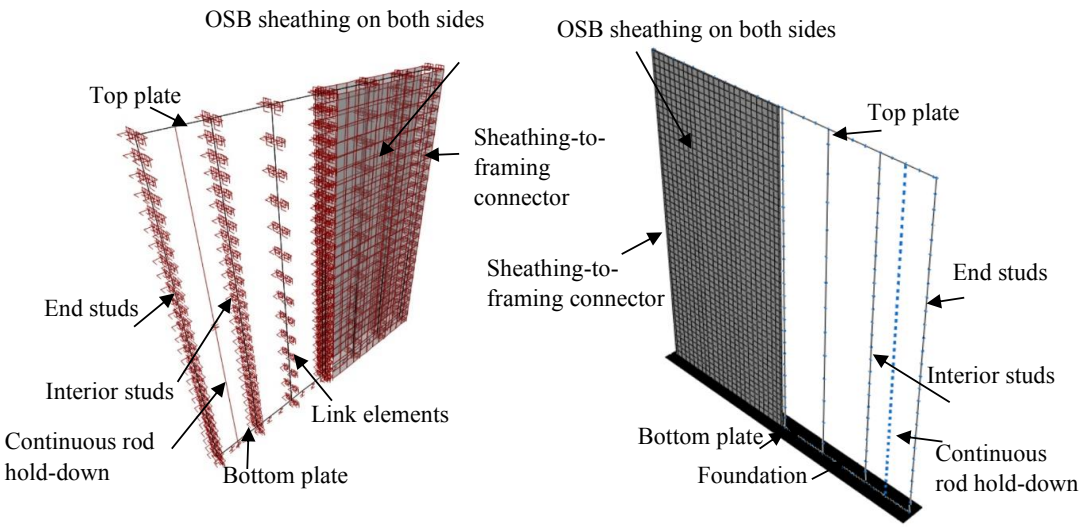

Figure 2. Schematic of finite element model of strong light-frame wood walls with continuous rod hold-downs: (a) SAP2000, (b) ABAQUS.

Table1. Material Properties for Radiata pine and OSB panels, obtained from [1,11,12].

Material Property	Radiata pine	OSB
E1 (MPa)	11400	5170
E2 (MPa)	1200	2980
E3 (MPa)	750	130
G12 (MPa)	869	1255.66
G12 (MPa)	797	1307.49
G23 (MPa)	142	128.16
$\boldsymbol{\nu_{12}}$	0.467	0.184
$\boldsymbol{\nu_{13}}$	0.456	0.364
$\boldsymbol{\nu_{23}}$	0.488	0.312

To simulate the behavior of the shear walls in SAP2000 [8], linear "frame" elements were employed to replicate framing members such as studs, bottom, and top plates, while "membrane" elements were used to model the sheathing panels. Similarly, in ABAQUS [9], 2-noded beam (B31) elements with six degrees of freedom at each node were used to model framing components. The sheathing panels were modeled shell (S4R) elements, which are 4-noded elements with six degrees of freedom at each node, and link (CONN3D2) elements were used to model sheathing-to-framing connections (see Figures 2 and 3).

As the contribution of framing-to-framing connection to the overall stiffness of the wall is small according to previous studies in this area, framing-to-framing connection were assumed as pinned connections [1]. To model framing-to-framing connections, moments were released in the frame element ends in SAP2000, and ties with free rotation constraints were defined in ABAQUS. Gap elements (defined as a type of “link” element in SAP2000) with high stiffness in compression were used, representing the foundation. Additionally, links with horizontal restraint represented the bolts connecting the wall to the foundation and preventing sliding. In ABAQUS software, a rigid foundation was added to the bottom to simulate high compression stiffness. The horizontal degree of freedom of the bottom plate was restrained to prevent wall sliding.

The wall response is mainly governed by the non-linear shear behavior of the connections between the sheathing and framing [1]. Sheathing-to-framing nails were modelled using nonlinear link connectors in SAP2000 (see Table 2). It is important to highlight that the nonlinear characteristics of the nail were distinctly defined for the two transitional degrees of freedom (DOF) of the nail, specifically those subjected to shear force in the plane of the wall. Modelling nails in ABAQUS is more challenging compared to those in SAP2000. Three sets of parameters were used to represent the nonlinear response of link connections in ABAQUS. Elastic properties with the linear stiffness, followed by plastic hardening behavior with nonlinear isotropic hardening using tabular data, and finally, damage properties based on relative plastic motion (where linear softening was assumed) were considered. These parameters are listed in Table 2.

The bottom boundary condition of the wall comprises hold-downs at both ends. To model the behaviour of the discrete hold-downs, a bi-linear elastic behaviour was considered in both software (see Figure 3). The links representing hold-downs have a tensile stiffness of k_t = 11.85 kN/mm (Figure 3(a)) according to test data for discrete hold-downs [4]. The continuous steel rods were modeled using link elements with a deformation response which is defined according to test data provided in Estrella et al. [6] shown in Figure 3 (b). Monotonic analysis (pushover test) was conducted by applying displacement-controlled loads to the top plate of the two walls.

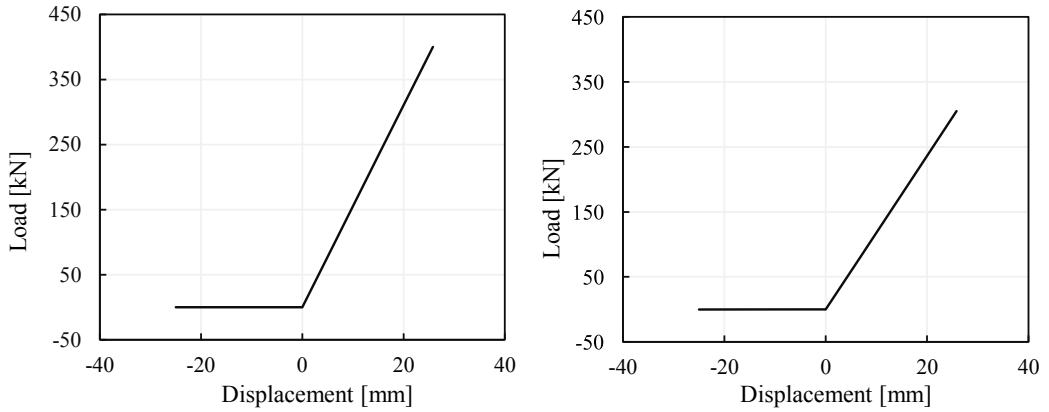

Figure 3. Multi-linear behavior of (a) continuous rod, (b) discrete hold-down described as input in SAP2000.

Table 2. Sheathing-to-framing connector properties used in (a) ABAQUS, (b) SAP2000 based on testing data reported in [4,6].

(a) ABAQUS		(b) SAP2000	
Elastic Parameters		Force (N)	Displacement (mm)
Stiffness (N/**mm²**)	Value	0	0
		100	0.11
D11	911	714	1.37
D22	911	879	2.07
D33	12	1040	3.78
Plastic Parameters		1290	7.83
Force (N)	Displacement (mm)	1470	11.95
714	1.37	1100	17
879	2.07		
1040	3.78		
1290	7.83		
1470	11.95		
Damage Parameters (mm)			
Plastic motion at damage initiation	11.95		
Plastic motion at failure	17		

RESULTS

The simulated load-displacement curves of the two strong shear walls with discrete and continuous rod hold-downs, are shown in Figures 4 and 5, respectively. Results are compared with testing data from experiments, another numerical model reported in the literature and analytical design equations provided in the Canadian Standard (CSA O86:2019). The load-displacement curves are compared with design equations to determine the accuracy range of the equations and their relevance to strong shear walls. As it was shown previously in Ghazi-Nader et al. [13] for low-capacity walls with the design values less than 20 kN, CSA design equation accurately predict the initial slope (wall stiffness). As it shown in this paper, for high-capacity walls, the design equations overestimate the initial wall stiffnesses slightly. However, the design equation is not able to capture the nonlinear trend quite accurately at higher lateral loads (~above 70kN). Therefore, the provisions of the CSA standard may have some inaccuracy levels when estimating the structural response of strong wood-frame walls, as they tend to underestimate deflections. This suggests further research is needed to relevance of current design equations for calculating inter-story drifts in multi-story buildings.

Figures 4 and 5 clearly show that the developed FE models in this study could capture the non-linear deformation, especially the softening response of strong shear walls under excessive displacements quite accurately. Hence, they could be used for assessing the damage response of wood-frame buildings constructed with stronger shear walls than conventional ones. It is envisioned that the developed models could serve as valuable tools for performing parametric investigations and understanding the nonlinear response of wood-frame shear walls built with various aspect ratios, stud, plate, and nail configurations.

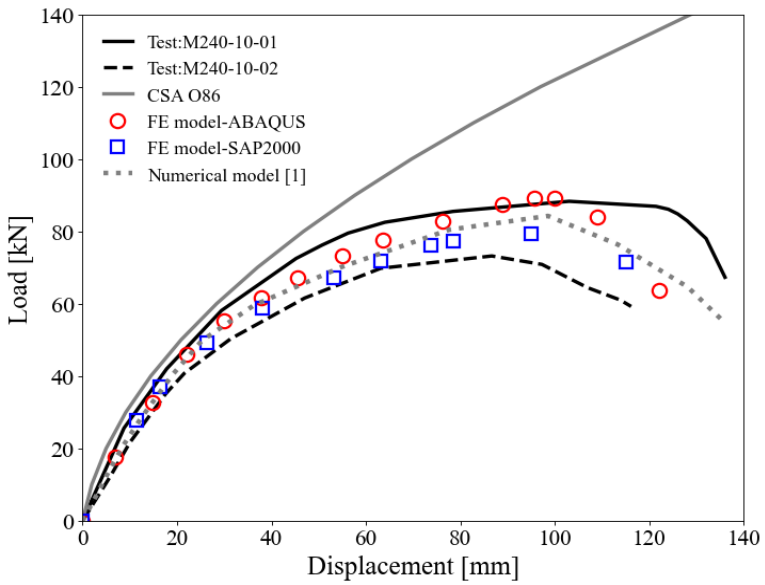

Figure 4. Comparison of load-displacement curves of the FE models with experiments, as well as analytical design equations CSA O86:2019 for strong light wood-frame shear wall with discrete hold-down.

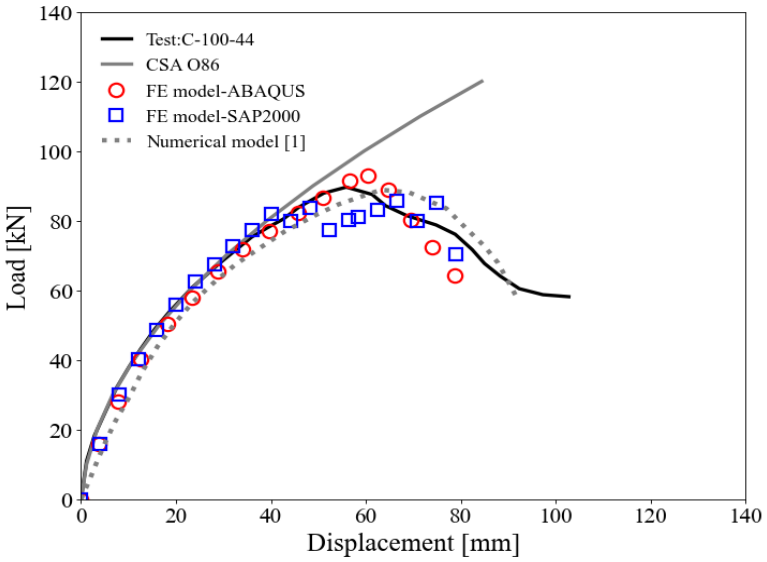

Figure 5. Comparison of load-displacement curves of the FE models with experiments, as well as analytical design equations CSA O86:2019 for strong light wood-frame shear wall with continuous steel rods.

CONCLUSIONS

The nonlinear deformation response of two types of strong shear walls with potential use in the construction of multi-story residential buildings were examined numerically in this study. Two detailed FE models were developed using beam, shell, and links elements in two commercial FE software packages and their accuracy were assessed using experimental data. Furthermore, the results were compared against Canadian Standard Association (CSA O86:2019) four-term design equation. Results demonstrate the accuracy of the developed numerical models in predicting the wall stiffnesses and capturing the softening response of walls up to failure at higher load levels. The design equations were shown to underestimate the deflection of strong shear walls (unlike conventional wood-frame shear walls) at higher lateral loads.

ACKNOWLEDGMENTS

The authors gratefully acknowledge the financial support of the University of Victoria (FGS Award) and Natural Sciences and Engineering Research Council of Canada (NSERC). Additionally, the authors thank the support of Dr. Chun Ni (FPInnovations), and Forestry Innovation Investment (FII) through the Wood First Program. Moreover, Dr. Xavier Estrella is acknowledged for providing experimental data on shear walls. Finally, Computers & Structures, Inc (CSI) is acknowledged for providing the SAP2000 software license.

REFERENCES

[1] Estrella, X., Guindos, P., Almazán, J. L., & Malek, S. (2020). Efficient nonlinear modeling of strong wood frame shear walls for mid-rise buildings. *Engineering Structures*, 215, 110670.

[2] APA-The Engineered Wood Association. (1996). Non-residential roof systems: design/construction guide. Tacoma, WA: APA-The Engineered Wood Association. 36 p.

[3] Countryman, D. (1952). Lateral tests on plywood sheathed diaphragms: Laboratory Report No. 55. Tacoma, WA.: Douglas-Fir Plywood Association.

[4] Guíñez, F., Santa María, H., & Almazán, J. L. (2019). Monotonic and cyclic behaviour of wood frame shear walls for mid-height timber buildings. *Engineering Structures*, *189*, 100-110.

[5] American Wood Council (AWC). (2015). Special Design Provisions for Wind and Seismic (SDPWS).

[6] Estrella, X., Malek, S., Almazán, J. L., Guindos, P., & Santa María, H. (2021). Experimental study of the effects of continuous rod hold-down anchorages on the cyclic response of wood frame shear walls. *Engineering Structures*, *230*, 111641.

[7] Engineering Design in Wood (CSA O86). (2019). Canadian Standards Association., Toronto, ON.

[8] Computers and Structures, Inc. (2024). CSI Analysis Reference Manual: SAP2000, ETABS and SAFE, Berkeley, CA.

[9] ABAQUS (2020) Analysis User's Manual. Dassault Systemes Simulia, Inc.

[10] Seim, W., Kramar, M., Pazlar, T., & Vogt, T. (2016). OSB and GFB as sheathing materials for timber-framed shear walls: Comparative study of seismic resistance. Journal of Structural Engineering, 142(4), E4015004.

[11] Malek, S., Zobeiry, N., Dai, C., & Vaziri, R. (2019). Strain-softening response and failure prediction in notched oriented strand board. Journal of Materials in Civil Engineering, 31(6), 04019094.

[12] Forest Products Laboratory (US). (1987). Wood handbook: wood as an engineering material (No. 72). The Laboratory.

[13] Ghazi-nader, D., Afshari, Z., Froese, T., Sun, M., & Malek, S. (2023). Deflection of wood-frame shear walls under large lateral loads: Analytical design equations versus experimental data. *CSCE Annual Conference - Moncton, NB.*

CALIBRATION OF CONCRETE DAMAGE PLASTICITY (CDP) PARAMETERS FOR NUMERICAL ANALYSIS OF REINFORCED CONCRETE STRUCTURE

Ch. Hymavathi Annapoorna[1#] and G. Appa Rao[2]

[1] PhD student, Department of Civil Engineering, Indian Institute of Technology, Madras.

[2] Professor, Department of Civil Engineering, Indian Institute of Technology, Madras.

Corresponding Author: Chandrabhatla Hymavathi Annapoorna.

Department of Civil Engineering, Indian Institute of Technology, Madras, Chennai, Indian, Pincode-600036

Email: *hymavathichandrabhatla@gmail.com.*

ABSTRACT

Assessment of structural response under extreme loading through advanced Finite Element analysis is very important. However, capturing the accurate response of Reinforced Concrete (RC) structures requires careful consideration of geometry, boundary conditions, and material characteristics. Despite well-established material models available for concrete and steel, the prediction of realistic structural response remains uncertain. Tests on uniaxial compression yield material parameters for concrete in compression, while establishing the parameters for concrete in tension through direct tension tests is quite challenging. Thus, inverse analysis and tests like three-point bend test, compact tension test etc., are being adopted to obtain softening parameters of concrete. An inverse approach through finite element modelling has been employed to optimize the softening parameters, emphasising Load-CMOD (crack mouth opening displacement) response on notched beams. The sensitivity of Load-CMOD response on $\sigma(w)$ $vs.w$ (cohesive stress-crack opening displacement) relationship to understand the efficacy of the proposed inverse analytical methodology in generating optimal $\sigma(w)$ $vs.w$ relation is focused. This work advances the understanding and modelling nonlinearity of concrete, thereby improving the accuracy of structural analyses.

Keywords: *Softening behaviour, Concrete Damage Plasticity, Fictitious crack model, multi-linear approximation*

1. INTRODUCTION

Concrete, as a primary construction material, exhibits complex fracture behavior characterized by strain softening which attributes to the stiffness degradation of concrete in tension. Accurate representation of concrete's softening behavior is essential for predicting structural responses using numerical modelling techniques. The fictitious crack model (FCM), pioneered by *Hillerborg [1]*, is the fundamental framework for understanding this nonlinear fracture phenomenon of concrete in tension. Within fracture process zone (FPZ), tension-softening constitutive model expressed by cohesive stress-crack opening displacement ($\sigma(w)\ vs.w$) relationship captures the intricacies of concrete fracture. However, obtaining precise $\sigma(w)\ vs.w$ response through uniaxial tensile tests is challenging as it requires sophisticated equipment and precise experimental set-up. To address this complexity, attempts have been made using indirect techniques such as wedge splitting (WS) and three-point bending (TPB) fracture tests as viable alternatives. However, $\sigma(w)\ vs.w$ relation cannot be established directly using such indirect techniques as the stress distribution is non-uniform unlike uniform distribution in uniaxial tension case. Thus, inverse analysis methodologies are developed for formulating softening response by comparing experimentally observed load – deflection or load – crack mouth opening displacement data.

Another approach to establish the $\sigma(w)\ vs.w$ relationship is by utilizing numerically developed load-deflection or load-crack mouth opening displacement (CMOD) response. Recently, several inverse analytical methods have been developed to extract $\sigma(w)vs.w$ relationship in concrete using bending or wedge-splitting tests, which can accurately characterize the tension-softening behavior of concrete improving understanding and modelling of concrete fracture properties. Inverse analysis is a technique in which the load - CMOD or load- deflection curves, experimental output is utilized in developing the softening relation of the material. In literature, Inverse analytical methods for establishing tension softening of concrete include J-Integral, poly-linear method and global optimization-based method. In J-Integral method, $\sigma(w)\ vs.w$ relation is obtained by numerical differentiation of the observed load, vertical displacement of the loading point and the crack tip opening displacement [2].

The poly-linear method pioneered by *Kitsutaka* [3], assumes $\sigma(w)vs.w$ relationship, which consists of a series of continuous piecewise linear functions. In this method, the $\sigma(w)vs.w$ relation is formed step-by-step as crack propagates by comparing the simulated load-CMOD curve with experimentally observed load-CMOD curve. As the relation is assumed to be poly-linear, this method does not require any initial approximation of the shape of the $\sigma(w)vs.w$ curve. However, the $\sigma(w)\ vs.w$ relation developed in each segment is sensitive to the measured values and the error in this approach is cumulative. An error in previous segment influences the entire $\sigma(w)\ vs.w$ relation. In Global optimization-based method the simulated (FE modelling techniques) or numerically (using analytical frame work) obtained load-deflection curve is fit to match the experimental load-deflection response presuming the shape of $\sigma(w)\ vs.w$ relation (linear, bi-linear, tri-linear, or exponential) [6]. Although this method overcomes the drawback of cumulative error in poly-linear method by adjusting the fitting

displacement. Behaviour of concrete in the linear elastic stage has been defined using elastic properties (Modulus of elasticity and Poisson's ratio). The concrete nonlinearity in the model is incorporated by Concrete Damage Plasticity (CDP) model. CDP includes defining plasticity, uniaxial compression, and uniaxial tension parameters. The failure mechanism in CDP model considers crushing of concrete incorporated as concrete compression hardening parameters and concrete cracking in tension defined by concrete tension stiffening parameters. The evolution of damage in concrete can be quantified through the damage parameter (between 0 and 1) in both compression and tension separately in terms of field variables like strains, and displacements.

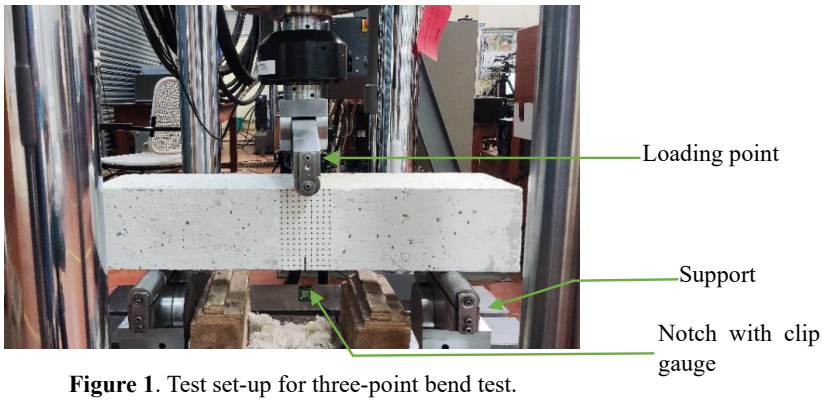

Figure 1. Test set-up for three-point bend test.

In the present study, the uniaxial compression parameters have been developed using the experimental results and the uniaxial tension specifically the softening of concrete have been developed as a function of displacement by the proposed inverse modelling approach. Further, other parameters like dilation angle of 35°, flow potential eccentricity of 0.1, the ratio of equibiaxial compressive yield stress-to-initial uniaxial compressive yield stress of 1.16, ratio of the second stress invariant on the tensile meridian-to-that on the compressive meridian of 0.67 and viscosity parameter of 0.0 is constant in the entire work.

3.1 Concrete Compression Hardening Parameters:

Uni-axial stress-strain behaviour of concrete can be simulated using the experimental data or by incorporating the stress-strain relations available. The accuracy in representing the behaviour of the concrete depends on the parameters adopted in developing the stress-strain relation. In this study, the stress (f_c) $vs.$ Strain $(\in_c)$ relation is expressed as a function of maximum stress (f_o) and corresponding strain $((\in_o)$ along with other parameters k, n_{asc} and n_{dsc} using Eqs. (1- 4) from the literature. The parameters (n, k, n_{asc} and n_{dsc}) are adjusted to align with the experimental results and behaviour predicted using the equations is shown in **Figure 2**. All the three equations showed good agreement up to peak stress with the experimental observations, while the post-peak response has been predicted well by Edric and Bikce [4-7] due to a separate parameter 'n_{dsc}' used for the post-peak response prediction.

In the equations, k, n_{asc} and n_{dsc} values have been optimised to match with the experimental stress-strain behaviour. In **Figure 2**, 1 for k, 1.6 for n_{asc} and n_{dsc} are chosen and the relations are drawn. It has been observed that Eqs.(3- 4) are in good agreement with the experimental results in the pre-peak and upto 45% of the maximum strain $(\in_{cmax})$ in the post-peak region. Though the prediction between $\in_o$ to $\in_{cmax}$ is not satisfactory, the prediction between

$0.7* \in_{cmax}$ to $\in_{cmax}$ improved as the value of n_{dsc} is adjusted to 2.7. Thus, the descending branch is predicted using two different values for n_{dsc} 1.6 between $\in_o$to $0.45 *\in_{cmax}$ and n_{dsc} 2.7 between $0.7 *\in_{cmax}$ to $\in_{cmax}$ in Eq. (4). Between $0.45 *\in_{cmax}$ to $0.7 *\in_{cmax}$ a transition curve has been fit using transition curve fitting. This is used in generating the input data (stress vs crushing strain) to ABAQUS [13] as shown in **Figure 3**.

$$f_c = f_o\left(\frac{\in_c}{\in_o}\right)\left(\frac{n}{n-1+\left(\frac{\in_c}{\in_o}\right)^n}\right) \tag{1}$$

$$f_c = f_o\left(\frac{\in_c}{\in_o}\right)\left(\frac{n}{n-1+\left(\frac{\in_c}{\in_o}\right)^{n*k}}\right) \tag{2}$$

For $0 \leq \in_c \leq \in_o$

$$f_c = f_o\left(\frac{\in_c}{\in_o}\right)\left(\frac{n_{asc}}{n_{asc}-1+\left(\frac{\in_c}{\in_o}\right)^{n_{asc}}}\right) \tag{3}$$

For $\in_o < \in_c$

$$f_c = f_o\left(\frac{\in_c}{\in_o}\right)\left(\frac{n_{dsc}}{n_{dsc}-1+\left(\frac{\in_c}{\in_o}\right)^{n_{dsc}}}\right) \tag{4}$$

Where

$n = (0.4 \times 0.001 \times 145.037 \times f_o) + 1$

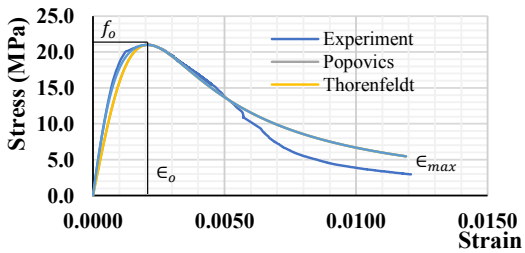

Figure 2. Stress-Strain relation for concrete using empirical expressions.

3.1 Tension softening behaviour

Post-peak response of concrete in tension is defined by specifying the stress as a function of strain or displacement or fracture energy (ABAQUS) [13]. It is difficult to execute the direct tensile test on concrete and thus indirect tensile tests like three-point bend, wedge splitting and compact tension tests, in which load vs. crack mouth opening displacement (CMOD) data is used to obtain the softening response (stress-displacement). The stress-displacement relation

can be represented either by a linear, bilinear, tri-linear, multi-linear or exponential relation as shown in Figure 5. In this study, multi-linear relation is assumed between stress and displacement. The stress here is the cohesive stress in Fracture Process Zone (FPZ) of fictitious crack model. The basic assumption of this model is that the concrete can transfer tensile force in FPZ until the crack opening width reaches a critical value, w_c. The value of the cohesive stress $\sigma(w)$ is equal to the tensile strength of concrete f_t where the corresponding displacement, w_o is zero. As w increases there would be drop in $\sigma(w)$, reaches zero when w reaches the critical value. Thus, the stress (cohesive stress in fictitious crack models) that can be transferred between $w_o$to w_c is assumed to be a multi-linear function of the crack opening displacement (w) which is represented by Eq. 5 [8].

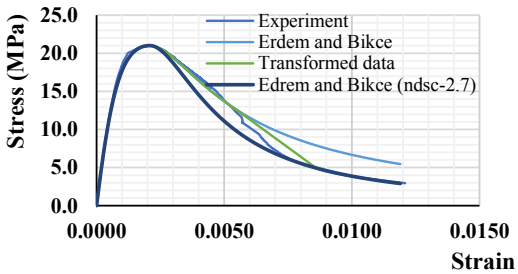

Figure 3. Comparison of Stress-Strain relation from *Edrem and Bikce* [4] equation to experiment data.

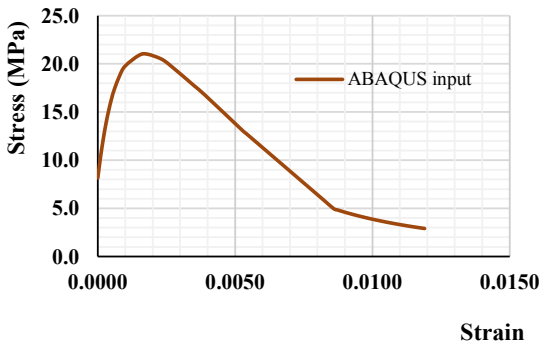

Figure 4. ABAQUS input for uni-axial compression behaviour

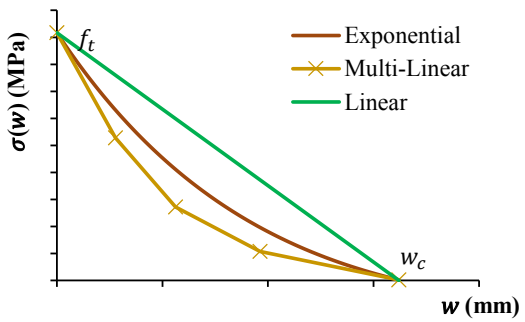

Figure 5. Strain softening relation for concrete.

$$\sigma(w) = b_i + (k_i w) \tag{5}$$

Here i takes the values of integers (1,2, 3 …. n) where n is the number of segments in the multi-linear model. The values of b_i and k_i are adjusted for each segment to predict the softening behaviour of concrete.

The degradation of concrete in both compression and tension is defined using the uncoupled compression damage and tensile damage parameters. In this study, as the softening parameters are obtained using three-point bend simulation, the compression damage is negligible when compared to the tensile damage and thus the compression damage parameters are not incorporated in this study. The tensile degradation is expressed by damage parameter (between 0 and 1) as a function of displacement as given in Eq. (6) [7].

$$d_t = 1 - \left(\frac{\sigma}{f_t}\right) \tag{6}$$

4. METHODOLOGY FOR DEVELOPING SOFTENING PARAMETERS:

In this section, an inverse analysis process using finite element modelling software (ABAQUS) [13] to develop the softening behaviour of concrete has been discussed. The optimisation of the parameters has a series of steps to be followed.

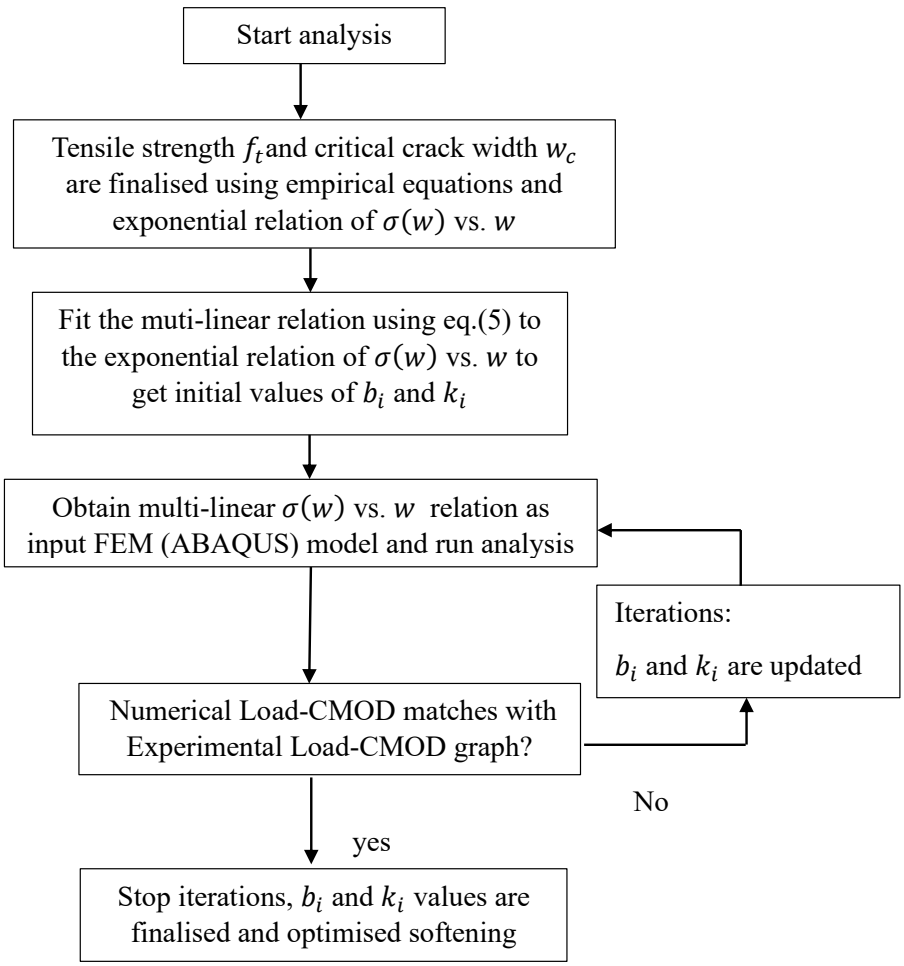

Figure 6. Flowchart for the proposed inverse analysis method

1. Initial approximation: Two points on the softening curve can be established if the critical crack length w_c and the tensile strength of the concrete are known prior. These two can be easily obtained either by experimentation or using the existing empirical equations. Here as an initial approximation Eqs. (7-8) are used to obtain the values of $f_t$and w_c. An initial exponential relation in Eq.(9) has been deployed and the load vs. CMOD response is extracted to compare with the experimental results. Further, f_t is adjusted using the initial exponential relation between $\sigma(w)$ and w [9-10] to agree with the observed peak load to the experimental peak load.

$$f_t = A\sqrt{f_c'} \tag{7}$$

A=0.33 – Initial approximation

$$w_c = 3.5\left(\frac{G_F}{f_t}\right) \tag{8}$$

$$G_F = \left(\frac{Area\ \ under\ load-CMOD\ curve}{(D-a_0)t}\right)$$

D- depth of the beam

a_o- initial notch depth

t-thickness of the beam

$$\sigma(w) = \left(1 - \left(\frac{w}{w_c}\right)e^{-2\left(\frac{w}{w_c}\right)}\right)f_t \tag{9}$$

2. First multi-linear approximation: In this step as an initial multi-linear relation is fit to the exponential curve using Eq.(5). The numerically obtained Load- CMOD curve is compared with the experimental Load-CMOD response.
3. Subsequent Iterations: The next iterations are continued by developing the $\sigma(w)$ vs. w relation by changing the slope of the multi-linear equation. In each iteration the developed relation is given as an input to the model and results are compared to the experimental results. Iterations are continued until optimum values of $\sigma(w)$ vs. w is obtained which can reciprocate the experimental Load-CMOD curve.

5. RESULTS AND DISCUSSION

In this section, the results obtained for each iteration are presented with detailed explanation:

Initial Approximation: In this step, the value of A in Eq.(7) is adjusted to capture the peak load and optimise the value of tensile strength f_t. It is observed from Figure 7 that a value of 0.4 for A gave good results for maximum load rather than 0.33 proposed by *Hillerborg* [1]. Thus, tensile strength of 1.833 MPa is established in this study by incorporating a value of 0.4 for A.

First Approximation: In this step, a multi-linear curve is fit to the exponential relation Eq.(3). It has been observed that numerical Load -CMOD response deviates from the experimentally observed Load-CMOD curve as shown in Figure 9.This confirms that the multi-linear model needs further optimisation of the parameters b_i and k_i in eq.(5) to obtain the exact softening behavior of concrete.

Subsequent Iterations: In the subsequent steps the slopes of the multi-linear equations are adjusted it can be observed from Figure 11 that a minor deviation in the softening parameters can primarily affect the Load-CMOD response.

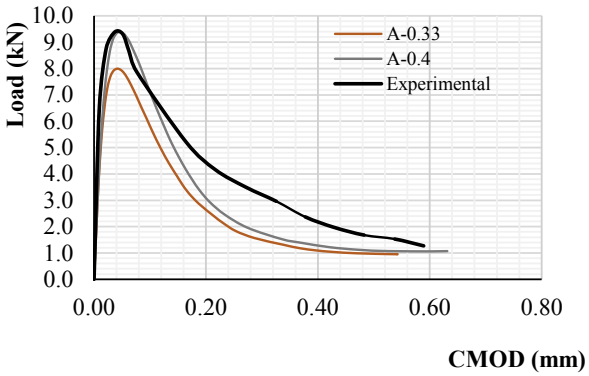

Figure 7. Load-CMOD curve for initial approximation.

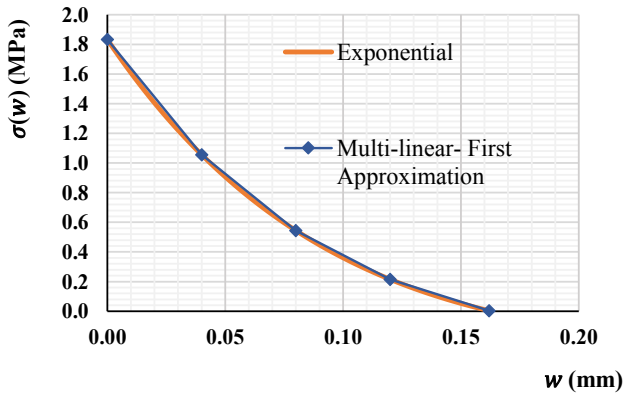

Figure 8. Softening parameters for first approximation.

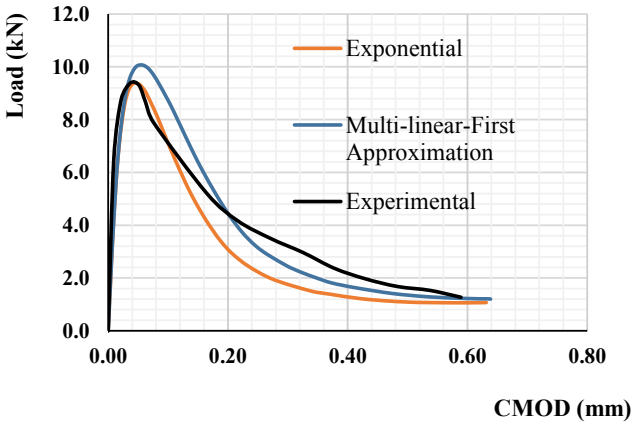

Figure 9. Load-CMOD curve for first approximation.

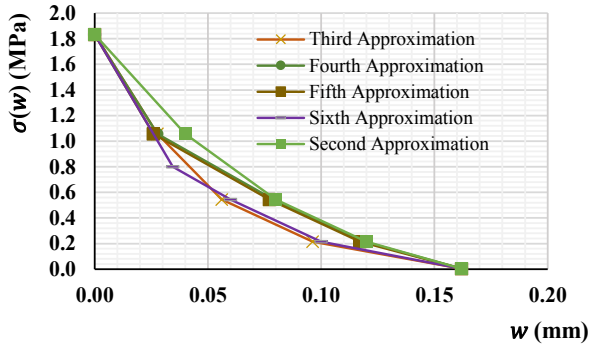

Figure 10. Softening parameters for subsequent iterations.

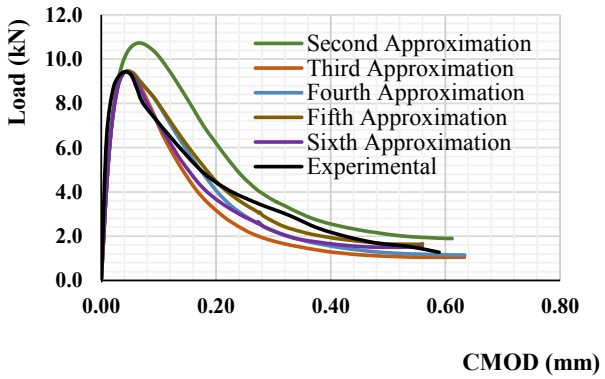

Figure 11. Load-CMOD curves for the subsequent iterations.

Final Iteration: For the slope values (-30, -8, -3, -1.5) in the multi-linear model, the input parameters for the numerical model are obtained and presented in **Error! Not a valid bookmark self-reference.**. The load-CMOD response obtained using these parameters is in good agreement with the experimentally observed Load-CMOD curve as shown in Figure 13. At this stage, no further iterations are carried out and the input relation $\sigma(w)$ vs. w is considered as the optimised softening behaviour of the concrete used in this study. This developed softening relation along with the damage parameters can be used in analysing the structures to quantify their behavior under different loading conditions.

Table 1 Softening input parameters for numerical modelling in final iteration.

Damage (d)	Stress (f) (Mpa)	Crack width(w) (mm)
0	1.833	0
0.563557	0.8	0.034433
0.781779	0.4	0.084433
0.882623	0.215152	0.146049
0.997944	0.003769	0.286971

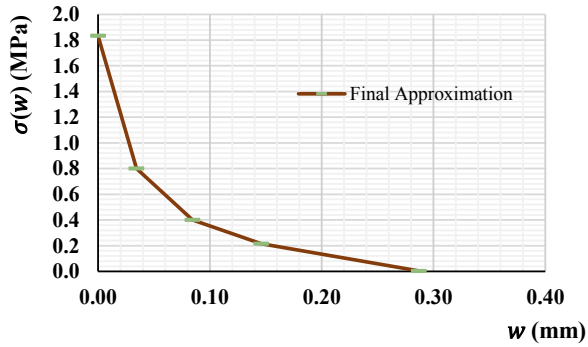

Figure 12. Softening parameters for the final iteration.

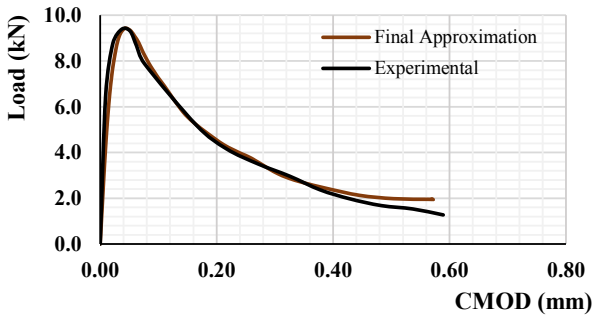

Figure 13. Load-CMOD curve for the final iteration.

6. CONCLUSIONS

The softening response of concrete has been developed using an inverse finite element modelling approach wherein the input parameters are optimized until the output matches well with the experimental results. The softening parameters have been optimized by considering the Load-CMOD response on a notched beam. This study also focused on generating the input for compression behavior of concrete for CDP model in ABAQUS[13]. From the study, the following conclusions have been drawn.

1. It has been observed that the stress-strain relation reported by *Edric and Bikce* [6] seems to be in good agreement with the experiment results up to the strain equal to 40% of maximum strain, by adopting individual parameters; n_{asc} for the ascending, and n_{dsc} descending branches in this model. The approach of dividing the descending branch using two values of n_{dsc} of 1.6 and 2.7 and introducing a transition trend in between resembles the experimental values.
2. Presumption of an exponential relation between $\sigma(w)$ vs. w for softening parameters and a value of 0.4 instead of 0.33 for A when tensile strength f_t expressed as a function of $\sqrt{f_c'}$ gave better maximum load prediction in three-point bend finite element model.
3. The Load-CMOD response has been observed to be sensitive to the type of $\sigma(w)$ vs. w relation. The $\sigma(w)$ vs. w relation, an input to the finite element model optimised

using proposed methodology of combined inverse analysis with global-optimisation approach yielded better agreement of experimental load-CMOD response to the load-CMOD response from finite element model.

REFERENCES

[1] A. Hillerborg, M. Modeer, P.E. Petersson, Analysis of crack formation and crack growth in concrete by means of fracture mechanics and finite elements, *Cement and concrete research* 6 (6) (1976) 773–781.

[2] V.Li, C.Chan, & C.K.Leung. (1987). Experimental determination of the tension-softening relations for cementitious composites. *Cement and concrete research*, 17(3), 441-452.

[3] Y. Kitsutaka, Fracture parameters by polylinear tension-softening analysis, *J. Eng. Mech.* 123 (5) (1997) 444–450.

[4] J.L.Sousa, & R.Gettu (2006). Determining the tensile stress-crack opening curve of concrete by inverse analysis. *Journal of engineering mechanics*, 132(2), 141-148.

[5] Mahmud, G. H., Yang, Z., & Hassan, A. M. (2013). Experimental and numerical studies of size effects of Ultra High Performance Steel Fibre Reinforced Concrete (UHPFRC) beams. *Construction and Building Materials*, 48, 1027-1034.

[6] Erdem, M. M., & Bikçe, M. (2021). Uniaxial stress–strain relation for low-and normal-strength concrete in compression. *Magazine of Concrete Research*, 73(16), 819-827.

[7] Popovics S (1973) A numerical approach to the complete stress–strain curve of concrete. *Cem Con Res* 3(5): 583–599, https://doi.org/10.1016/0008-8846(73)90096-3.

[8] Desayi, P., & Krishnan, S. (1964, March). Equation for the stress-strain curve of concrete. *ACI Journal Proceedings* (Vol. 61, No. 3, pp. 345-350).

[9] Thorenfeldt, E. (1987). Mechanical properties of high-strength concrete and applications in design. *In Symposium Proceedings, Utilization of High-Strength Concrete*, NR, 1987.

[10] Mi, Z., Hu, Y., Li, Q., Wang, Y., Zhang, H., & Zhang, Z. (2023). An inverse analysis method for determining tensile softening relationship of concrete considering local response. *Construction and Building Materials*, 394, 132195.

[11] Najafgholipour, M. A., Dehghan, S. M., Dooshabi, A., & Niroomandi, A. (2017). Finite element analysis of reinforced concrete beam-column connections with governing joint shear failure mode. *Latin American Journal of Solids and Structures*, 14, 1200-1225.

[12] Han, X. Y., Wu, Z. M., Jia, M. D., Zheng, J. J., & Rena, C. Y. (2023). A new method for determining the tension-softening curve of concrete. *Theoretical and Applied Fracture Mechanics*, 126, 103992.

[13] Smith, M. (2009). *ABAQUS/Standard User's Manual, Version 6.9*. Dassault Systemes Simulia Corp.

FINITE ELEMENT MODELING OF BEAM-TO-COLUMN CONNECTIONS IN TALL MASS TIMBER BUILDINGS

Dina Ghazi-nader[1], Jacci Rock[2], Kyle Stueck[2], Roger Parra[2], Parham Khoshkbari[3] and Sardar Malek[4]

[1*] Department of Civil Engineering. University of Victoria, Canada

[2] Degenkolb Engineers, San Francisco, California, USA

[3] Google LLC, Mountain View, California, USA

[4*] Assistant Professor, Department of Civil Engineering. University of Victoria, Canada

Corresponding Author: Sardar Malek
Department of Civil Engineering, University of Victoria, Victoria, BC V8P 5C2, Canada.
[*]Centre for Advanced Materials and Related Technology (CAMTEC), University of Victoria, 3800 Finnerty Rd, Victoria, BC, V8P 5C2, Canada.

Email: smalek@uvic.ca

ABSTRACT

Advances in timber engineering and the manufacturing of laminated timber products have facilitated the adoption of mass timber as a sustainable construction material with a reduced carbon footprint in taller construction projects. Special detailing is essential at beam-to-column connections in these buildings to support both gravity and lateral loads while minimizing damage to the timber columns and beams. In general, the gravity connections between beams and columns are designed to withstand shear forces. Nevertheless, in the event of an earthquake, these connections must exhibit the ability to undergo substantial lateral deformations and rotations, while preserving their load-carrying capacity. Limited research has been dedicated to BTC connections subjected to both moments and shear forces. This paper aims to assess the behavior of glulam BTC connections under both lateral and gravity loads with the objectives of quantifying the impact of gravity load on the lateral stiffness of the system and examining the deformed shape of connection components. To achieve this goal, a three-dimensional numerical model of the glulam BTC connection has been developed. Results showed the ductile performance of connections due to yielding of clip angle screws. The predicted large stresses implied the high risk of screw withdrawal and splitting in glulam columns under lateral loads. The developed model not only enables designing future large-scale experiments but also overcomes limitations associated with experimental testing.

Keywords: *Mass timber, Glulam, Connection, Yielding, Gravity system, Finite Element Method*

INTRODUCTION

As the height of mass timber buildings continues to rise in the world, the demand for resilient high-capacity gravity connections compatible with lateral force-resisting systems (LFRS) intensifies. While recent years have witnessed the emergence of innovative solutions to resists lateral loads, challenges persist in devising reliable, ductile beam-to-column (BTC) connection systems [1, 2]. Gravity connections in mass timber buildings are often required to be hidden, fire-proofed and exhibit high ductility to ensure reliable transfer of gravity loads in an earthquake event. This highlights the imperative for enhanced design approaches for resilient gravity systems.

From a structural design perspective, the bending capacity and deformation behavior of conventional timber beams and columns and conventional timber connection systems with nails and screws have been well-investigated in the literature. However, determining the capacity of more advanced and proprietary connection systems at higher lateral loads, due to the large number and arrangements of screws being used to connect mass timber products has not been well-studied.

In mass timber construction, hidden connections are often preferred by architects. They should demonstrate high fire-proofing rating and maintain the aesthetic of exposed timber members. For bearing and hanger connections, this can be obtained by using a “knife plate” connection – or a connection where a thin plate gets set into the end of a mass timber member. Timber plugs could be used under the steel plate that supports the beam to create an “invisible” connection which protects the steel elements from fire hazards.

As a first step towards providing a better understanding of the behaviour of hidden gravity BTC connections, a simple custom-designed connection system proposed for mass timber buildings in the literature (see [3, 4]) has been selected in this paper. The authors believe that this simple connection is less expensive than most proprietary connectors and is much easier to install. However, deformation compatibility of this gravity connection with lateral systems is worth a careful investigation. The selected connection involves a glulam beam that is framed into the side of a glulam column through a steel knife plate. This beam sits on the horizontal section of the steel plate. The vertical section of the steel plate is screwed to the side of the column which undergoes a lateral movement. Employing a three-dimensional finite element (FE) model, the connection behaviour is investigated numerically and compared with reported test data in the literature. For this purpose, the whole system is subject to combined lateral and gravity loads, and the lateral load-displacement curve of the connection is predicted and compared to experimental data.

Results demonstrate the significant effect of the gravity load, the orthotropic mechanical properties of glulam members, and the imposed boundary conditions on the connection stiffness. Notably, the loading direction, end support conditions, and the magnitude of the gravity load are studied and shown to have significant effect in connection design.

METHODOLOGY

The selected connection testing setup in [3] consisted of 3.66 m glulam column, connected to glulam beams. The glulam beam had a depth of 610 mm, width of 311 mm and extended 4270 mm from the column face. Both beams and columns were made of 24F-V4 Douglas Fir glulam timber [5]. The base of the glulam column was supported by a pin connection (consisted of a steel bar), and the end of beam was supported by a roller support. The beam end support is simulated by applying vertical constraints and assigning symmetric boundary conditions to the orthogonal faces of the glulam beam (see Figure 1).

It should be noted that four different connection systems and their behaviours under the combined lateral and gravity loads were tested in the literature [3-6]. Among those, the experiment with a knife plate connection (C1-KP) consisted of a Grade A36 steel plate which was screwed into the column [3,4] has been selected and modelled. The beam itself was notched to account for the knife plate. A clip angle was used to ensure maintaining a connection between the beams and columns under lateral loads (i.e. prevent sliding the beam off the steel plate). Two screws were used to install the clip angle and connect it to beams and columns, respectively.

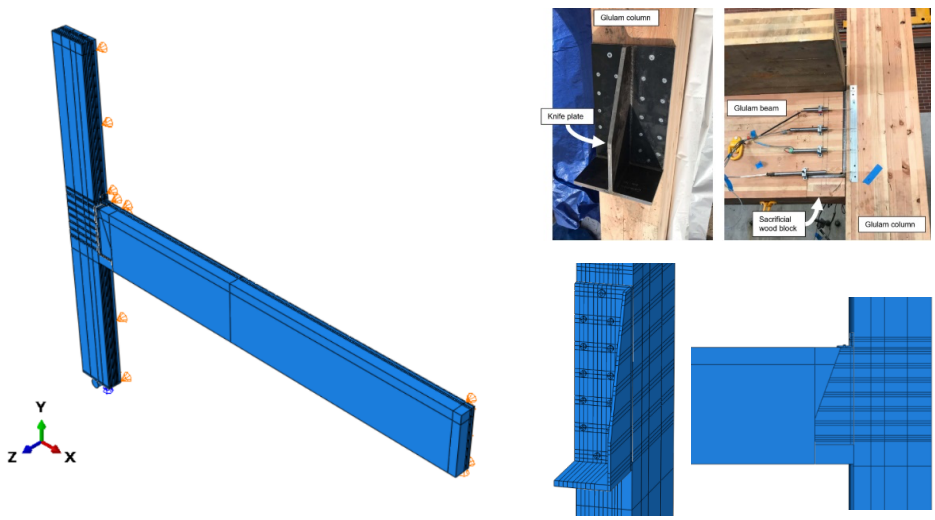

Figure 1. Finite element model for the BTC connection: (a) 3D view; (b) knife plate and assembled connection described in [3,4]. Half of the connection has been modelled due to symmetric boundary conditions.

To reduce the computational time and due to symmetry, half of the experimental setup described above is modelled. The 12 screws that are used to screw the knife plate to column were modelled using solid elements. Full bonding is assumed between the screws and the corresponding surfaces holes in the column to ensure tight bonding between the screw and the timber. Frictionless contacts are assumed between the glulam beam and the knife plate surfaces. The top of the beam is connected to the column face using the two screws and the clip angle. A frictionless contact between the steel clip angle and the glulam surfaces is considered in the simulations.

The analysis starts by applying the gravity load to the beam followed by applying a lateral (horizontal) load to the top of column. Half of the experimental gravity load is applied to a line defined in the geometry module of the FE software. First, a ramp gravity load is applied while the column end is free to move. Once the full gravity is applied, a horizontal load is applied to the deformed shape of the model in the second step. The lateral load is applied to the top edge of the column while its displacement is monitored during the loading step. It should be noted that two cases are considered for the lateral load. The lateral load is applied to the top of the column in the positive direction first to study the behaviour of the connection during a pushing phase (see Figure 2). The load is then reversed, and the column is pulled in the negative direction to examine the performance of the connection during pulling (see Figure 3). The predicted lateral load-deformation curves in these two cases are compared and presented in the results section. Once the model is validated for the gravity load applied in the testing, a parametric study is conducted with a range of gravity loads to examine the effect of gravity load magnitude on the connection initial stiffness.

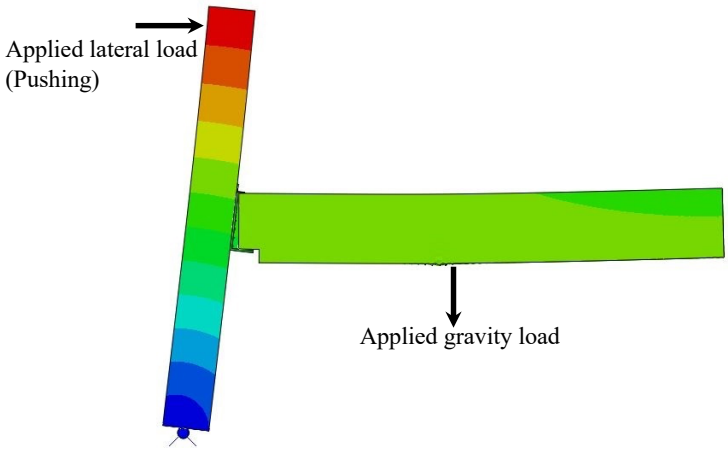

Figure 2. Deformed shape of the glulam beam and column during pushing phase.

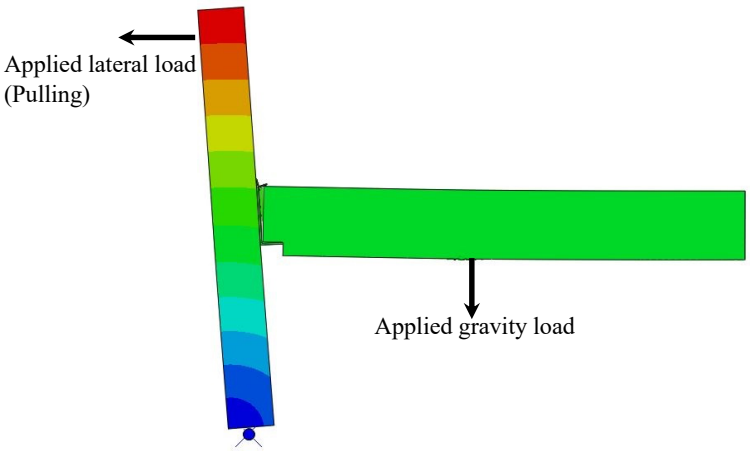

Figure 3. Deformed shape of the glulam beam and column during pulling phase.

RESULTS

The simulated load-displacement curves of the select BTC under pushing and pulling scenarios are provided in Figure 4. The test results are also provided with the numerical results for comparison. The numerical results represent the nonlinear response qualitatively, although they underestimate the load, especially in pulling. This discrepancy might be attributed to factors such as the presence of a deck on the beam during experimentation, which was not accounted for in the numerical model, as well as experimental errors. It should be noted that the timber is assumed to be an orthotropic elastic material in the current version of the model while steel components are defined as elastic-plastic to elucidate the effect of plastic deformation in the clip angle screws. The induced pulling forces in the screws and the high stresses generated perpendicular to grain direction of timber demonstrate the high potential of screw withdrawal and development of small cracks/splitting in the timber as reported in the experiments. These damage mechanisms contribute to softening response of the connection under excessive lateral loads and degradation of connection stiffness noted in both pushing and pulling cycles.

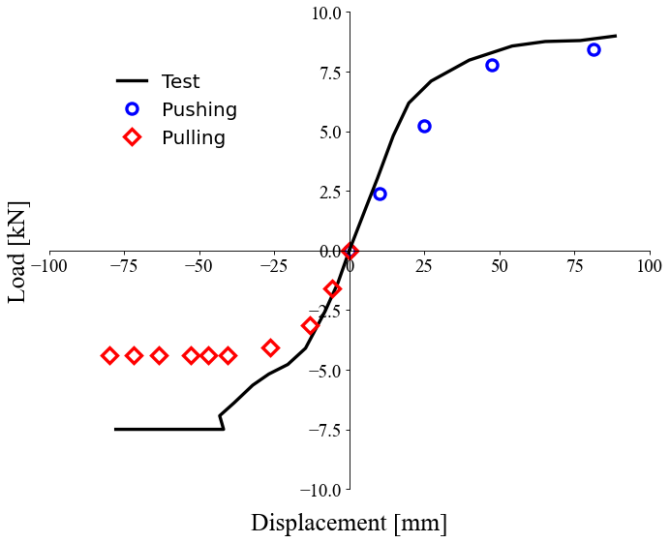

Figure 4. Lateral load-displacement behavior of the BTC during pulling and pushing phases.

In terms of connection stiffness, results show the effect of loading direction on the initial connection stiffness which requires further attention for structural design. Furthermore, numerical results highlight that the magnitude of the gravity load have a significant effect on the connection behavior. To study this further, four different load levels were examined: 76 kN (the gravity load used in the experiment), 38 kN (50% of the full load), 19 kN (25% of the full load), and 7.6 kN (10% of the full load) as depicted in Figure 5. The corresponding initial connection stiffnesses are also listed in Table 1. The findings show that as the gravity load increases, the initial stiffness of the BTC connection decreases. In addition, increasing the gravity load level reduces the maximum strength of the connection. As testing various connection systems connecting glulam members with different sizes and under a range of gravity loads is quite costly, conducting virtual tests using the developed FE model seems to

be a reasonable approach to design connections with an optimized performance for tall mass timber buildings.

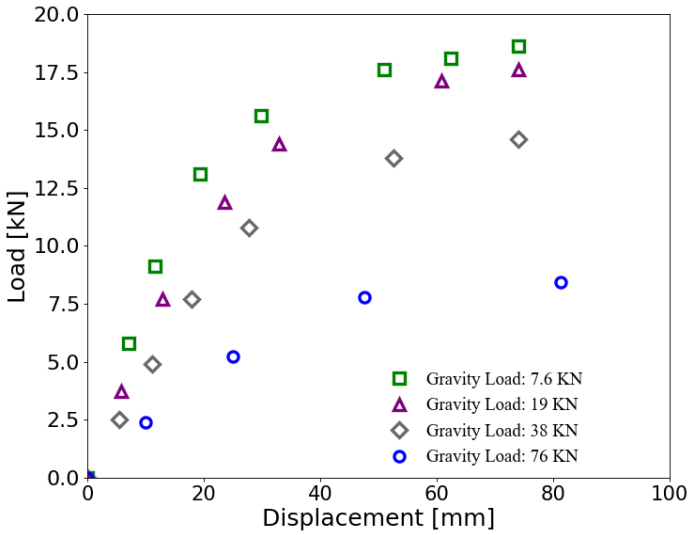

Figure 5. The effect of gravity load level (where both gravity and lateral loads are applied simultaneously) on the lateral load-displacement behavior of the BTC during pushing phase.

Table 1. Predicted initial stiffness of the BTC connection at various gravity load levels. The measured initial stiffness of the connection under the gravity load of 76.5 kN, is 365 N/mm based on experimental data.

Gravity load level (kN)	Initial Stiffness k_{i+}(N/mm)
7.6	721
19	593
38	441
76	237

The stress contours shown in Figure 6 and 7, show that the ductile performance of the connection is mainly arising from the plastic deformation of the clip angle screws while the knife plate is still undergoing elastic deformation (see Figure 7). In terms of deformed shape, similar deformed shape for screws reported in the experiments [3] highlights the relevance of the FE model in capturing the deformed shape of connection details. Furthermore, the predicted stress distribution in the timber members, proves the elastic deformation of timber along the grain direction while screws are undergoing yielding. In contrast, high perpendicular to grain stresses in the column between the screws connecting the knife plate to the column side are noted. Such large stresses emphasizes the importance of the proper spacing between screws to prevent splitting in the columns under extreme lateral loads (e.g. earthquake events). It is

envisaged that the developed model be used in quantifying and comparing such stresses under similar loading scenarios for different bearing and hanger connection systems. Further testing and model improvement (e.g. by incorporating sophisticated damage models) are required to ensure the accuracy of the model in such scenarios.

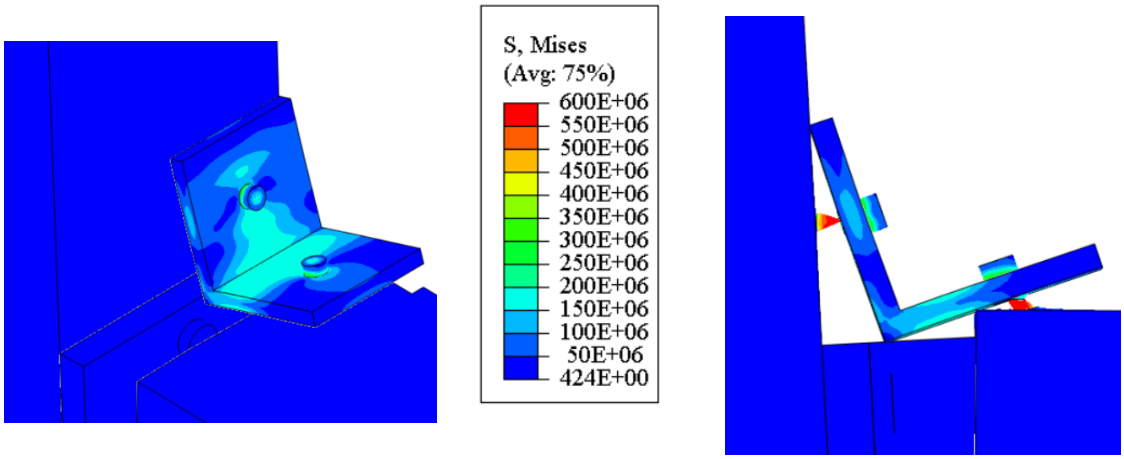

(a)

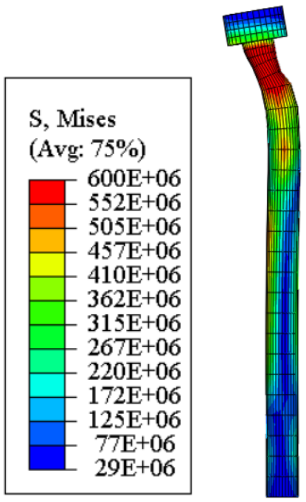

(b)

Figure 6. Deformed shape and von-Mises stresses (in Pa) in the (a) clip angle and (b) typical screw during pulling.

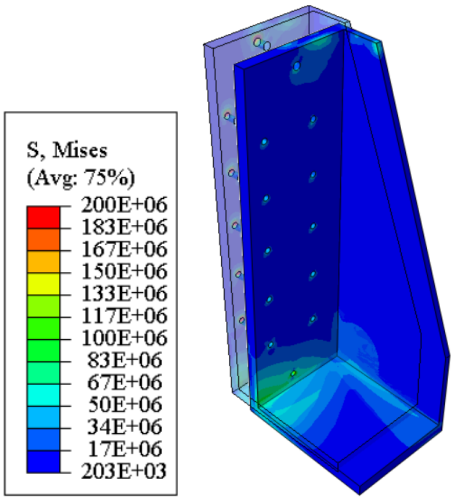

Figure 7. Steel knife plate undeformed (hidden black line) and deformed shape after pushing. The colour plot shows the von-Mises stress (in Pa) distribution in the plate. Half of the plate is shown due to symmetric boundary conditions.

CONCLUSIONS

A FE model was developed to examine the performance of BTC systems under complex loading conditions as an alternative to costly laboratory testing. The numerical results provided valuable insights into the nonlinear response of connections under lateral loading and onset of yielding in the screws. The loading direction (pushing versus pulling), connection detailing (e.g. screw and clip angle location), and the magnitude of gravity load, were shown to play significant roles in determining connection stiffness and overall ductility of the connection system.

The predicted stress contour in the screws and steel plates revealed the ductile performance of connections due to yielding of clip angle screws, while highlighting the importance of screw spacing to prevent column splitting under extreme lateral loads. The study underscores the high risk of screw withdrawal and splitting in glulam columns, emphasizing the need for more resilient connection systems and their further testing to ensure maintaining structural integrity of mass timber buildings in seismic events.

This research demonstrated the value of conducting a more comprehensive study of the behaviour of BTC connections using detailed 3D FE models. Remedies for safeguarding the structural integrity and protecting mass timber structures, particularly in seismic regions such as the west coast of Canada and the USA, need further research involving combined experimental-numerical approaches.

ACKNOWLEDGMENTS

The authors gratefully acknowledge the financial support of the University of Victoria (FGS Award) and Natural Sciences and Engineering Research Council of Canada (NSERC). Ariel

Creagh from Degenkolb Engineers is acknowledged for providing valuable insights during the course of this project.

REFERENCES

[1] Busch, A., Zimmerman, R., Pei, S., McDonnel, E., Line. P., Huang, D. (2022) Prescriptive seismic design procedure for post-tensioned mass timber rocking walls. *Journal of Structural Engineering,* 148(3):04021289.

[2] He, M., Luo, Q., Li, Z., Dong, H., Li, M. (2018) Seismic performance evaluation of timber-steel hybrid structure through large-scale shaking table tests. *Engineering Structures*, 175, 483–500.

[3] Madland H., Fischer, E., & Sinha. A. (2023b) Monotonic testing of glue-laminated beam-to-column connections, *Journal of Structural Engingeering,*149, 4.

[4] Madland, H., Fischer, E. C., & Sinha, A. (2023). Cyclic Testing of Glue-Laminated Beam-to-Column Connections. *Journal of Structural Engineering*, *149*(4), 04023013.

[5] American Wood Council (AWC). (2018) National design specification for wood construction. NDS, Leesburg, VA.

[6] Zimmerman, R.B., & Mcdonnell, E. (2017) Framework-A tall re-centering mass timber building in the United States. In: *New Zealand Society for Earthquake Engineering Conference*. Wellington, New Zealand.

PROTECT2024